On-Chip Adiabatic Demagnetisation Refrigeration

Francis Ciarán Bettsworth, MPhys (Hons)

A thesis submitted for the degree of *Doctor of Philosophy*

Physics Department

Lancaster University

February 2024

Declaration

I declare that the work presented in this thesis is, to the best of my knowledge and belief, original and my own work. The material has not been submitted, either in whole or in part, for a degree at this, or any other university. This thesis does not exceed the maximum permitted word length of 80,000 words including appendices and footnotes, but excluding the bibliography. A rough estimate of the word count is: 15471

Tuesday 20th February, 2024

Francis Ciarán Bettsworth

On-Chip Adiabatic Demagnetisation Refrigeration

Francis Ciarán Bettsworth, MPhys (Hons).

Physics department, Faculty of Science and Technology, Lancaster University

A thesis submitted for the degree of *Doctor of Philosophy*. February 2024

Abstract

This thesis describes the thermal modelling and simulation of on-chip adiabatic demagnetisation refrigeration. On-chip cooling is a novel refrigeration technique which has been developed to solve the apparent poor thermalisation of electrons in microkelvin nanoelectronics. Micrometre- and nanometre-scale electronics are fundamental to the development of quantum technologies and hot electrons often degrade the performance of these devices. Microkelvin electron temperatures,will allow for the investigation of new physical phenomena and exotic electronic states of matter. Prior to this work, microkelvin electron temperatures have been produced by a combination of on-chip and off-chip refrigeration. The combination of cooling elements obfuscates the importance and necessity of off-chip cooling components. Without a complete description of on-chip cooling thermal dynamics, this combination of techniques also complicated the optimisation of on-chip refrigeration. This thesis presents a first-principles thermal model and simulation of on-chip demagnetisation refrigeration. This work finds that the thermal dynamics of a coulomb blockade thermometer with on-chip cooling are well-captured by this model. Using the simulation, this work explores the limits, constraints and optimisation of on-chip cooling. The results of this exploration outline a path towards microkelvin electrons in a 10 mK refrigerator with on-chip demagnetisation cooling.

Publications

The following publication was generated while developing this thesis from data and simulations included in this thesis. Portions of this work are used in chapter 3 in particular.

S. Autti, **F. C. Bettsworth**, K. Grigoras, D. Gunnarsson, R. P. Haley, A. T. Jones, Y. A. Pashkin, J. R. Prance, M. Prunnila, M. D. Thompson, and D. E. Zmeev, "Thermal transport in nanoelectronic devices cooled by on-chip magnetic refrigeration," *Physical Review Letters*, vol. 131, no. 7, p. 077 001, Aug. 17, 2023. DOI: 10.1103/PhysRevLett.131.077001

The following publication was generated while developing this thesis. Its content is relevant to ongoing and future work developed in conjunction with the simulation which forms the main body of this thesis.

M. Arrayás, **F. Bettsworth**, R. P. Haley, R. Schanen, J. L. Trueba, C. Uriarte, V. V. Zavjalov, and D. E. Zmeev, "Progress on levitating a sphere in cryogenic fluids," *Journal of Low Temperature Physics*, Feb. 4, 2023, ISSN: 1573-7357. DOI: 10.1007/s10909-022-02925-3

Contents

List of Figures

List of Tables

Chapter 1

Introduction

Experiment-based research in condensed matter and quantum technologies is largely dependent on access to low-temperature environments. Dilution refrigerators [3] , first realised in 1965 [4], have made millikelvin temperature accessible for a wide variety of experiments [5]. Dilution refrigeration, to this day, remains the workhorse of research at millikelvin temperatures [6]. The state of the art bespoke refrigerators can achieve continuous helium temperatures as low as 1.75 mK [7]. There is a worldwide shortage of helium and much uncertainty concerning the future supply of this resource, essential to low temperature research [8, 9]. The demand for millikelvin temperatures and low helium consumption has led to the development of 'dry' dilution refrigerators where first-stage cooling is produced by a pulse-tube refrigerator instead of helium evaporation [10–12]. There are now easily-accessible commercial solutions for dry dilution refrigeration with base temperatures around 10 mK [13] and easy access to low temperatures has opened the millikelvin regime to new research avenues [14, 15].

Commercial dilution refrigerators make 10 mK to 100 mK environments easily attainable with continuous cooling in this temperature range. There is however no convenient widely-applicable solution for cooling experiments to the submillikelvin regime. Adiabatic nuclear demagnetisation of copper has long been the workhorse

of achieving micro-, nano- and picokelvin temperatures [5, 16, 17] but extracting cooling power from the refrigerant becomes progressively more difficult with electron-phonon coupling weakening as temperature decreases [18]. Poor thermalisation of those systems, electronic systems in particular, have historically restricted conduction electron temperatures to above 4 mK [19–22]. Electron temperatures in nanostructures and quantum dots have been seen to decouple form the refrigerator, their temperature almost 100 mK above the dilution temperature [23].

On-chip adiabatic demagnetisation cooling has emerged as a technique for realising microkelvin electron temperatures in nanoelectronics [22]. This technique integrates small demagnetisation elements with the circuitry of a device, removing the need to cool through traditional thermal link of electron-phonon coupling [24–26]. On-chip cooling, in combination with off-chip demagnetisation, has produced microkelvin electron temperatures and hold times of multiple hours [27, 28]. Demagnetisation experiments in Lancaster have pursued cooling with on-chip nuclear refrigerant as the only cooling below dilution refrigeration [22]. With this approach, electron temperatures have been measured down to 1.0 ± 0.1 mK. The different institutions, while all using on-chip cooling to cool a Coulomb blockade thermometer, have taken differing approaches to refrigeration and thermalisation prior to on-chip cooling. In particular, both Delft and Basel used off-chip demagnetisation elements to refrigerate lead wires separately from the experiment. Demagnetisation of measurement leads was not included in Lancaster's experiments. The differences in off-chip methods and thermalisation points make it difficult to directly compare and evaluate the cooling power, potential and limits of on-chip demagnetisation alone.

This thesis describes first-principles thermal modelling and development of a simulation of on-chip demagnetisation cooling. Firstly a map or network the thermal baths, systems, and connections inside a magnetic refrigerant is described. External

electronic and phononic heat leaks are added to this network to form a thermal model of on-chip demagnetisation refrigeration. Secondly, this work builds a numerical simulation of temperature evolution in on-chip cooling using this model. The simulation is then compared to previous experimental measurements of on-chip cooling with Coulomb blockade thermometers (CBTs), highlighting how the cooling is well captured by the model without describing CBT dynamics. This thesis then uses the simulation to explore the constraints and optimisation of on-chip cooling. Lastly, this work explores the deposition of indium as a refrigerant for future on-chip cooling experiments.

The theory of adiabatic demagnetisation is described in chapter 2. This chapter also describes thermalisation and thermometry of electrons at millikelvin temperatures and presents a thermal model of on-chip demagnetisation cooling. In chapter 3 a simulation of the cooling of the chip is built and compared to demagnetisation experiments. A parameter-space exploration of on-chip cooling optimisation is performed in chapter 4 using this simulation. Chapter 5 describes progress made towards cooling a thin-film thermometer and experimental developments in indium electrodeposition. Finally, chapter 6 contains a summary of this thesis and thesis and presents and outlook for future work.

Chapter 2

Background

This chapter explores the necessary theory and research upon which this work is built. The chapter starts with a review of the physics and equations governing demagnetsation cooling. It then sets up the picture of electron thermalisation in low-temperature experiments and the inherent problems therein which this work sets out to solve. Following on from that are reviews and explanations of electron coolers, thermometers and details of previous research into cooling electron baths to milli- and submillikelvin temperatures for comparison with demagnetisation cooling.

2.1 Demagnetisation Cooling

Magnetic cooling is a technique for producing cooling power through the magnetic spin entropy and magnetocaloric effect [29] of paramagnetic systems. The technique was first used to cool significantly below 1 K by demagnetisation of electronic magnetic moments in paramagnetic salts. The temperature limits and difficulties in using paramagnetic salt cooling [30] have led to nuclear magnetic moments in quadrupolar metals, and in particular copper, being the system of choice for submillikelvin demagnetisation cooling [5]. Quadrupolar metals are not the only type of refrigerant in modern use with the Van Vleck paramagnet $PrNi_5$ also a notable coolant, owing to a higher cooling capacity than copper at higher temperatures [16]. It has also been suggested that paramagnetic electrons in highly doped semiconductors can be demagnetised for cooling, at temperature ranges similar to paramagnetic salts [31]. The primary limit or disadvantage of demagnetisation cooling is that it is a single-shot technique, so cannot indefinitely keep an experiment at or below a required temperature. Paramagnetic demagnetisation cooling is still the workhorse of submillikelvin cooling to this day [32] with a current research focus on adapting the technique to cryogen-free dilution refrigerators [33, 34] and multi-stage systems for near- or pseudo-continuous cooling [35–37]. There is also interest in extending the applicable temperature range of magnetic cooling to be useful near room temperature [38].

2.1.1 Entropy of paramagnetic nuclear moments

Consider a solid containing a system of non-zero nuclear magnetic spins. At a sufficiently low temperature, the interaction energy between these spins and the host lattice will cause the spins to spontaneously order into a zero-entropy state. If average thermal energy is much greater than the spin interaction energy the spins will be

free to create a randomly oriented system of dipoles. An external magnetic field will introduce an energetically preferred orientation of the dipoles, polarising and reducing the entropy of the spins. A stronger field will increase the polarisation and lead to magnetic ordering at higher temperatures [5]. With both temperature and magnetic field able to induce ordering, the entropy of this spin system can then by controlled by temperature and field. The contribution of dipoles to the entropy of the solid is given by $R\ln(2I+1)$ per mole of spins, where R is the ideal gas constant and $2I+1$ represents the number of possible dipole orientations and thus spin degeneracy. The total angular momentum quantum number for nuclear magnetic spins is conventionally represented by I. In an ideal nuclear paramagnet, interactions between moments can be ignored and the energy of the moments described by Zeeman splitting. The Zeeman splitting energy of dipoles in an applied magnetic field of strength B is given by

$$\epsilon_m = -\mu_\mathrm{n} g_\mathrm{n} m B \tag{2.1}$$

for single-occupancy energy levels $-I \leq m \leq I$, nuclear magneton μ_n and Landé nuclear g-factor g_n. The partition function is thus given by

$$Z = \left[\sum_{i=-I}^{I} \exp -\frac{-\epsilon_i}{k_\mathrm{B} T}\right]^{nN_\mathrm{A}} \tag{2.2}$$

for n moles of dipoles. N_A is the Avogadro number, k_B is the Boltzmann constant and T is temperature of the spin system. The entropy S and magnetisation M of this system can be found from

$$S = k_\mathrm{B} \frac{\partial T \ln Z}{\partial T} \tag{2.3}$$

and

$$M = k_{\mathrm{B}} T \frac{\partial \ln Z}{\partial B}. \tag{2.4}$$

The population of the the m'th energy level is given by

$$\mathscr{P}(m) = nN_{\mathrm{A}} \exp\left(-\frac{\epsilon_m}{k_B T}\right) / \sum_{m=-I}^{I} \exp\left(-\frac{\epsilon_m}{k_B T}\right). \tag{2.5}$$

Using equations (2.3) and (2.2) and some hyperbolic identities, the entropy can be written as

$$\frac{S}{Nk_{\mathrm{B}}} = \frac{x}{2I} \coth \frac{x}{2I} - \frac{2I+1}{2I} x \coth \frac{2I+1}{2I} x + \ln\left(\frac{\sinh \frac{2I+1}{2I} x}{\sinh \frac{x}{2I}}\right) \tag{2.6}$$

where

$$x = \frac{\mu_{\mathrm{n}} g_{\mathrm{n}} I B}{k_{\mathrm{B}} T} \tag{2.7}$$

and R is the ideal gas constant equal to $N_{\mathrm{A}} k_{\mathrm{B}}$. Similarly, equations (2.4) and (2.2) give

$$M/M_s = \frac{2I+1}{2I} \coth \frac{2I+1}{2I} x - \frac{1}{2I} \coth \frac{x}{2I} \tag{2.8}$$

where $M_s = nN_{\mathrm{A}} \mu_{\mathrm{n}} g_{\mathrm{n}} I$ is the saturation magnetisation.

The small value of the nuclear magnetic moment [$\approx 5 \times 10^{-27}\,\mathrm{J\,T^{-1}}$] typically leads to a Zeeman energy ϵ of much less than the average thermal energy $k_{\mathrm{B}} T$ [16]. Provided that the finite final field strength and spin temperature are sufficiently high to avoid magnetic self-ordering of spins, the value of the pre-factor x is also significantly smaller than average thermal energy, $\mu_{\mathrm{n}} g_{\mathrm{n}} I B \ll k_{\mathrm{B}} T$. Hence it is appropriate to use small angle approximations and series expansions for sinh and coth. Equations (2.6) and (2.8) can

thus be simplified to

$$S = nR\ln(2I+1) - \frac{n\lambda_{\mathrm{n}}}{2\mu_0}\frac{B^2}{T^2} \tag{2.9}$$

and

$$M = \frac{n\lambda_{\mathrm{n}}}{\mu_0}\frac{B}{T} \tag{2.10}$$

where $\lambda_{\mathrm{n}} = N_{\mathrm{A}}\mu_0\mu_{\mathrm{n}}^2 g_{\mathrm{n}}^2 I(I+1)/3k_{\mathrm{B}}$ is the molar Curie constant. Using the definition of heat capacity in a constant magnetic field

$$C_B = T\left(\frac{\partial S}{\partial T}\right)_B, \tag{2.11}$$

the nuclear spin heat capacity C_{n} can be calculated from equation (2.9) as

$$C_{\mathrm{n}} = \frac{n\lambda_{\mathrm{n}}B^2}{\mu_0 T^2}. \tag{2.12}$$

2.1.2 Adiabatic demagnetisation refrigeration

Figure 2.1 depicts a demagnetisation cycle used for refrigeration. Nuclear spins in a block of refrigerant are first magnetised in good thermal contact with a dilution refrigerator along path A to B. The heat release of magnetisation is absorbed by the dilution refrigerator and the spins cool to a low-entropy state close to the base temperature of the dilution stage. This temperature is the initial temperature for demagnetisation. The refrigerant is then thermally isolated from the dilution stage, commonly via a superconducting heat switch [16], and adiabatically demagnetised along path B to C. The temperature of the spin system greatly reduces with this demagnetisation. The cold spins now absorb heat and warm up to a high entropy

state along path C to D. This is where the cooling power of adiabatic demagnetisation is produced. Heat will be absorbed from any hotter experiment or device thermally connected to the refrigerant and the nuclear refrigerant will stay cold until its heat capacity is exhausted. Any heat leaks during demagnetisation will erode the cooling power of the refrigerant and limit the final temperature of demagnetisation.

Equations (2.6) and (2.9) show that spin entropy is a function of the variables field strength and temperature in the ratio B/T, with all other factors being material constants. An adiabatic condition implies that entropy must be constant and thus the ratio B/T must also be constant. This leads to the useful relation between initial and final states of

$$\frac{B_{\text{initial}}}{T_{\text{initial}}} = \frac{B_{\text{final}}}{T_{\text{final}}}. \tag{2.13}$$

Thus demagnetising magnetic spins will reduce their temperature with a final temperature given by

$$T_{\text{final}} = T_{\text{initial}} \left(\frac{B_{\text{final}}}{B_{\text{intial}}} \right). \tag{2.14}$$

The temperature-field relation holds true for non-interacting magnetic nuclear spins in the absence of any heat leaks and only under adiabatic conditions. The lowest possible temperature in demagnetisation is ultimately limited by the magnetic ordering temperature. In copper, this ordering temperature is less than 100 nK [39, 40]. When demagnetising to very small fields, the Zeeman splitting energy becomes sufficiently small that interactions between magnetic or electric nuclear moments can no longer be ignored. While remaining above the conditions for magnetic spin ordering, interactions between moments can be modelled as effective residual magnetic field b, internal to the material. This interaction can be accounted for by changing the applied field strength,

B into an effective field strength B_{eff} where

$$B_{\text{eff}} = \sqrt{B^2 + b^2} \tag{2.15}$$

and b is the strength of the residual internal field. The residual field is negligible at high magnetic fields. As $B \to 0$, the residual field dominates and limits the final temperature. The effective residual fields of some refrigerants can be found in table 2.1.

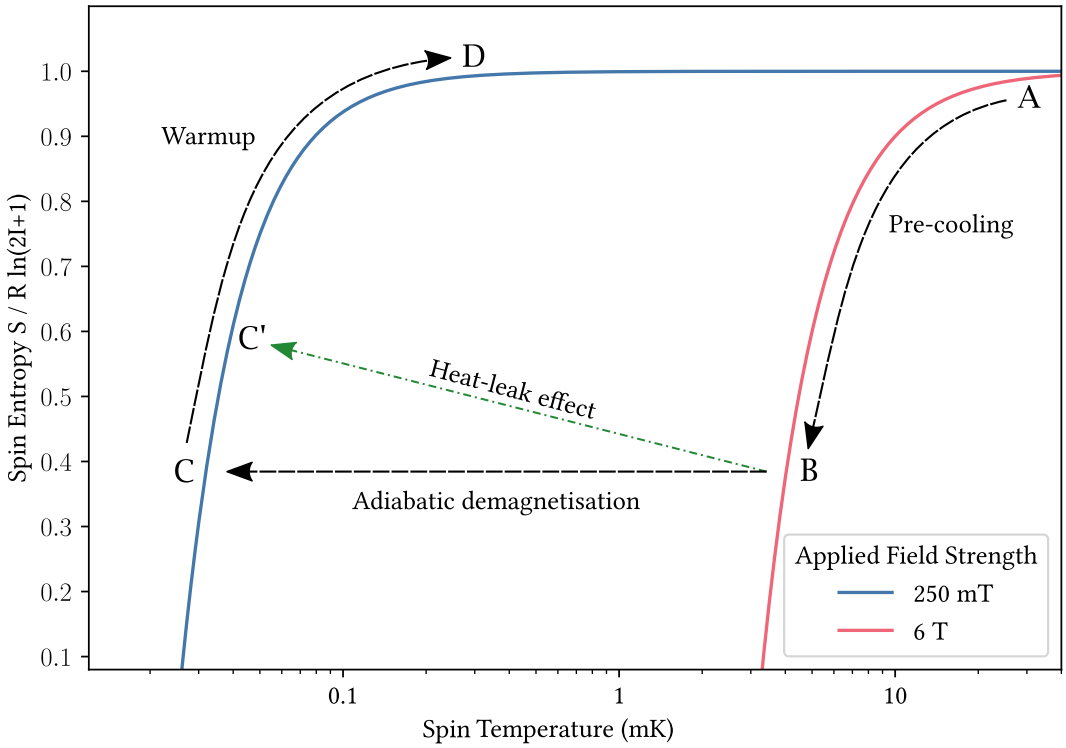

Figure 2.1: Illustrative diagram of the demagnetisation cycle. The spins are magnetised and cooled by a dilution refrigerator along path A to B. The spin system is then disconnected from the fridge and demagnetised along path B to C. As the spins return to equilibrium magnetisation along path C to D, providing a cooling power given by equation (2.19). Any heat leaks present during demagnetisation will shift the final spin temperature from the ideal C to C', reducing the resulting cooling power of the system.

2.1.3 Electron-nuclear heat flow

Adiabatic demagnetisation is effective in cooling nuclear spins to low temperatures. In order to use this technique to cool an experiment, there needs to be a strong thermal link between experiment and nuclear spins. Nuclear spins and conduction electrons readily share energy via spin-spin hyperfine interactions [16]. A relaxation time for this process, τ_1, can be defined as

$$\frac{d}{dt}\left(\frac{1}{T_\mathrm{n}}\right) = -\frac{1}{\tau_1}\left(\frac{1}{T_\mathrm{n}} - \frac{1}{T_\mathrm{e}}\right) \tag{2.16}$$

where T_n and T_e are the nuclear spin and conduction electron temperatures respectively. This relaxation time is highly material-dependent. Only electrons near the Fermi energy contribute to this interaction and their population is a function of T_e [32]. This leads to the Korringa law

$$\tau_1 T_\mathrm{e} = \kappa \tag{2.17}$$

where κ is a constant, independent of temperature, known as the Korringa constant and a measure of the hyperfine coupling. The constant has a field dependence close to the internal residual field and is constant for $B \gg b$. Equation (2.16) can be rewritten using this constant to give

$$\frac{dT_\mathrm{n}}{dt} = \frac{T_\mathrm{n}}{\kappa}\left(T_\mathrm{e} - T_\mathrm{n}\right). \tag{2.18}$$

The heat flow from electrons to nuclear spins, in the absence of external heat leaks is given by

$$\dot{Q}_\mathrm{e,n} = C_\mathrm{n}\frac{dT_\mathrm{n}}{dt} = \frac{C_\mathrm{n}}{\kappa}\left(T_\mathrm{e} - T_\mathrm{n}\right)T_\mathrm{n} = \frac{\lambda n}{\mu_0 \kappa}\frac{\left(B^2 + b^2\right)}{T_\mathrm{n}}\left(T_\mathrm{e} - T_\mathrm{n}\right) \tag{2.19}$$

using equations (2.18), (2.12), (2.15), the definition of heat capacity, the fact that $dC_n/dt = 0$ and that $C_n \gg C_e$.

2.1.4 Thermalisation in nuclear demagnetisation cooling

After adiabatic demagnetisation, the nuclear spins will be the coldest system in the whole refrigerator cryogenic environment. The challenge of running devices and experiments at low temperature is in building a thermal link between spins and experiment to extract cooling power, without compromising the operation of the devices nor the refrigerant.

A direct electrical connection between a device made of normal metal and a bulk nuclear demagnetisation stage would be the simplest thermal link for cooling device electrons. Direct electrical connections are not feasible for junction-based devices such as coulomb blockade thermometers where junctions could be shorted by the direct link or damaged when exposed to eddy currents in the stage during demagnetisation. As a result, such devices are typically cooled through strongly resistive or superconducting thermal links where phonons provide thermal transport in lieu of conduction electrons.

This direct electrical connection can be described at low temperatures using the Wiedemann-Franz heat law with an effective thermal resistance R_{WF} of

$$R_{WF} = \frac{3}{\pi^2}\left(\frac{e}{k_B}\right)^2 \frac{R}{(T_e + T_{device})/2} \tag{2.20}$$

where e is the electron charge, T_{device} is the electron temperature of the device and R is the electrical resistance of the interface [22].

Below 1 K and below the Debye temperature of a material, conduction electrons share energy with the host lattice by absorption and emission of phonons. Electron-phonon scattering is highly depended on lattice structure, impurities, and electronic structure in the material [41]. The heat flow between electrons and phonons of

temperatures T_e and T_p can be approximated as [42]

$$\dot{Q}_{e,p} = \Sigma V\left(T_e^q - T_p^q\right) \tag{2.21}$$

for electron-phonon interactions in a volume V with material coupling constant Σ. The temperature power q can vary greatly depending on material with experimentally observed values of $2 \leq q \leq 5$ [21, 43]. For many materials relevant to demagnetisation cooling, $q = 5$ [16, 18, 41, 42]. Values of the coupling parameter, Σ, can be calculated from known material constants [42] but these calculations often disagree with measurements [44]. This study uses measured values for Σ where possible.

Phonon-phonon heat flow across a boundary between two materials experiences a Kapitza resistance to heat flow [45–47]. The heat flow across and interface between two materials, $\dot{Q}_{pp}$ with phonon temperatures of T_x and T_y is given by

$$\dot{Q}_{x,y} = \left(T_x - T_y\right)/R_K = \left(T_x + T_y\right)^2\left(T_x^2 - T_y^2\right)\frac{A}{8r_K} \tag{2.22}$$

where r_K is the Kapitza resistance specific to the interface with surface area A [48]. A combined Kapitza resistance, R_K, representing a resistance to phonon transport across multiple stacked interfaces is given by $r_K = R_K A T^3$ using the approximation $T = \left(T_x + T_y\right)/2$ [1].

2.1.5 Choice of refrigerant

While the temperature reduction of adiabatic demagnetisation is largely independent of material [equation (2.13)], the resulting cooling power, thermalisation rate, susceptibility to heat lakes and minimum possible temperature vary greatly with changing material properties. The desirable properties for a nuclear refrigerant are:

1. A low Korringa constant κ such that electrons and nuclear spins thermalise

rapidly.

2. High curie constant λ_n for a large reduction in entropy, high cooling power and high heat capacity.

3. Large thermal conductivity such that the cooling power can be used to refrigerate experiments and devices.

4. Limited residual internal field to maximise $B_{final}/B_{initial}$.

5. No superconductivity at B_{final} to avoid the heat release of the transition and the absence of electronic thermal conduction in the superconducting state.

Desirable mechanical and metallurgical properties are also commonly added to selection criteria since the nuclear stage in traditional demagnetisation cooling is formed of large elements of bundled wire or large rigid blocks with vanes cut into them to reduce eddy current heating [5]. A refrigerant for this type of demagnetisation stage must be structurally sound and easy to machine into the required shape. For on-chip refrigerant used in this study, the refrigerant is not a structural component and is deposited lithographically so mechanical properties are much less of a concern. This opens up possibilities to explore new refrigerants or using paramagnetic semiconductors as substrate and refrigerant [31]. The relevant parameters and properties for a number of candidate refrigerants are shown in Table 2.1.

Quadrupolar metals are not the only options for refrigerants. There is also potential to use solid ^{3}He but many of the parameters required to model this are not yet known [49].

Material	T_f 10^4K	κ s K	λ pK m^3 mol^{-1}	b mT	I	Σ GW/m^{3}K^5	H_c mT
Cu	8.16	1.1	4.08	0.36	3/2	2.4	
In	10.0	0.086	17.4	250	9/2	41.22	30
Tl	9.46	0.0044	3.6		1/2		20
Sc	4.96	0.09	13.5	0.22	7/2		
Nb	6.18	0.19	21.7		9/2		300
Al	13.6	1.8	8.68		5/2	0.3	10
V	7.32	1.8	15.9		5/2		10

Table 2.1: Properties and parameters relevant to adiabatic demagnetisation performance for a number of different materials. The Fermi temperature is used to calculate the electronic heat capacity and is derived from Ashcroft and Mermin [50]. Electron-phonon coupling constant Σ comes from measurements of copper and aluminium [51] except for the value for indium which is calculated from theory [44]. All other values taken from Lounasmaa [5] except for scandium [52] and thallium [53].

2.2 Electron thermalisation and cooling

Electron-phonon heat flow and phonon conduction across material interfaces weaken with falling temperatures. At millikelvin temperatures these weak thermal links lead to poor thermalisation of electrons in devices with experimental heat leaks overpowering cooling. Thus it is common for electrons to have measured temperatures significantly above the host refrigerator temperature [18, 42]. One proposed solution for this thermalisation problem is to integrate small elements of demagnetisable material directly into circuitry and devices. These elements provide direct electrical thermalisation between refrigerant and device electrons, removing the need for cooling via phonons.

2.2.1 A thermal model of on-chip demagnetisation cooling

Figure 2.2 shows a scheme for thermalisation with on-chip nuclear refrigerant. A block or island of demagnetisable material, in this case made of copper, is lithographically deposited on a multi-layered substrate. This substrate sits upon a sheet of silver which is

assumed to be well-thermalised with a dilution refrigerator's mixing chamber. Phonons in the silver sheet have a temperature $T_{\mathrm{p,Ag}}$ equal to the mixing chamber temperature T_{MXC}. The island itself has three separate thermal systems: conduction electrons *e*, magnetic nuclear spins *n* and phonons *p*. These internal systems have their own temperatures $[T_{\mathrm{e}}, T_{\mathrm{n}}, T_{\mathrm{p,Cu}}]$ and heat capacities $[C_{\mathrm{e}}, C_{\mathrm{n}}, C_{\mathrm{p,Ag}}]$. The nuclear and phonon systems both share heat with conduction electrons at a rate moderated by a thermal resistances R_{en} and R_{ep}. There is a heat flow between the island phonons and phonons in the silver strip. The numerous interfaces between island and silver have individual boundary resistances. These are combined into a total effective thermal resistance to phonon heat flow, R_{pp}. A constant-power heat leak, Q_0, flows into the conduction electrons.

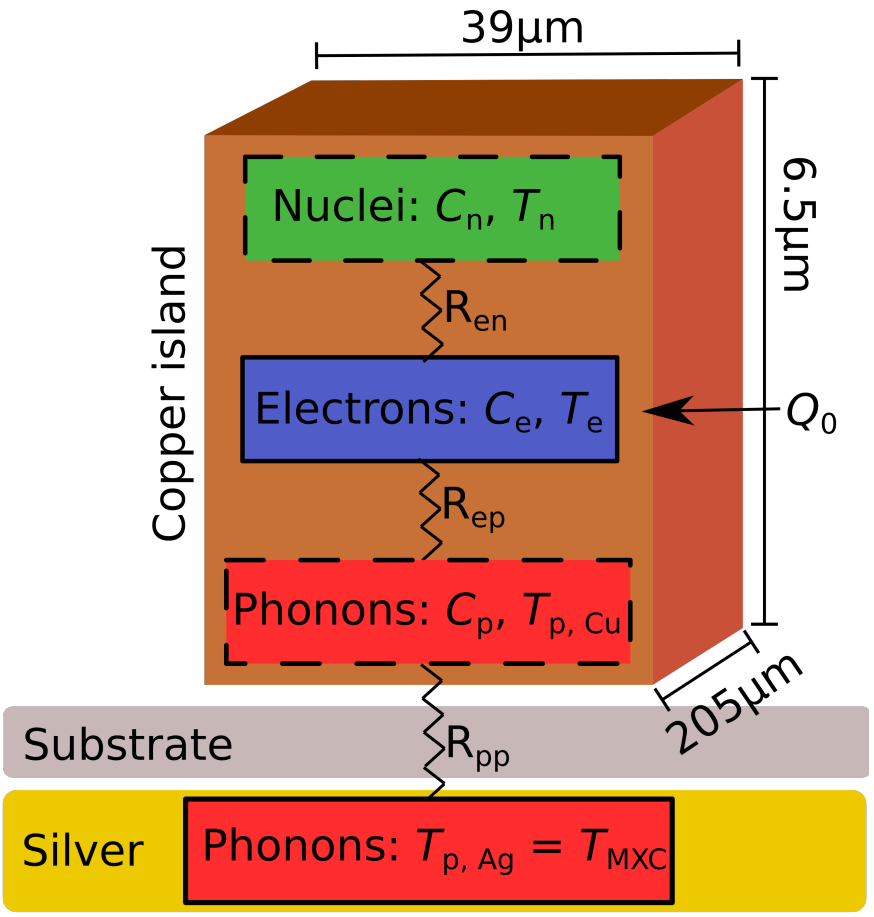

Figure 2.2: A schematic of the thermal links involved in on-chip demagnetisation. A block of copper contains three different thermal systems with their own heat capacities and temperatures: conduction electrons e, magnetic nuclear spins n and phonons p. Electron-nuclear heat flow is moderated by a thermal resistance R_{en}. Similarly, heat flow between electrons and phonons has a coupling resistance R_{ep}. The island is placed upon a multi-layered insulating substrate, separating the island from a silver plate. The silver plate is well thermalised with a dilution refrigerator with mixing chamber temperature T_{MXC}. Phonons conduct heat between the island and silver phonons via a combined Kapitza resistance R_{pp}. The electron system is heated by an external heat leak Q_0.

2.2.2 On-chip cooling and thermometry

On-chip adiabatic demagnetisation has seen recent success in cooling Coulomb blockade thermometers (CBTs) to submillikelvin temperatures [22]. A coulomb blockade thermometer is a primary thermometer formed by arrays of tunnel junctions [21]. The electrical conductance across the array depends on conduction electron population and temperature [51, 54]. With all tunnel junction thermometers there is an energetic limit imposed by the charging energy, across junctions [14]. Only electrons with thermal energy greater than this limit can take part in thermal transport. As temperature decreases, the population of electrons meeting the energy criterion also decreases. This leads to lower conductance across the junction and eventually total Coulomb blockade when no electrons are energetic enough for transport.

The construction of Coulomb blockade thermometers makes them ideal for investigating on-chip demagnetisation cooling. Islands of demagnetisable material can be grown between the tunnel junctions, integrating the cooling directly into an electron thermometer [24]. Such thermometers with integrated cooling have proven highly sensitive to electron temperature even below 1 mK [22] with the potential to measure temperature below 50 μK [28].

Using an indium on-chip refrigerant, CBTs have measured temperatures down to 421 ± 35 μK in combination with off-chip demagnetisation cooling of lead wires [27]. A similar approach of on- and off-chip demagnetisation cooling [22] has measured temperatures as low as 224 ± 7 μK using copper nuclear refrigerant. Lancaster CBT experiments have on-chip refrigerant as the only cooling below dilution refrigeration and do not use a heat switch to isolate the thermometer from the dilution stage [55]. Demagnetisation refrigeration with this on-chip only approach has resulted in measured electron temperatures of 1.0 ± 0.1 mK [1]. The thermalisation of a Lancaster CBT experiment is shown in subsection 2.2.1.

While effective in cooling into the microkelvin regime, the combination of on- and off-chip cooling makes it difficult to evaluate the performance of on-chip cooling alone. Comparing the mixed-cooling approaches with Lancaster's on-chip only approach raises a question of necessity. Does on-chip cooling require off-chip refrigeration to maximise cooling performance and how necessary is on-chip cooling for microkelvin electron temperatures?

2.3 Alternatives to on-chip demagnetisation cooling

On-chip demagnetisation cooling seeks to solve the electron thermalisation problem by integrating refrigeration with nanoelectronics and circuitry. This is far from only approach to lower electron temperatures and on-chip cooling may perform best when combined with other techniques, as evidenced by the record-low electron temperatures seen in Basel CBT experiments [22, 25, 28].

2.3.1 Immersion cooling.

A long-standing technique for thermalisation and cooling of experiments to temperatures below dilution refrigeration is liquid helium immersion. The device or experimental system is immersed in liquid ^{3}He, ^{4}He or some mixture of the two. For cooling below dilution temperatures, adiabatic demagnetisation is used to cool a metal in thermal contact with the liquid helium. The solid-liquid interface between copper and helium has notoriously-poor heat transfer which is described by the Kapitza resistance of the interface [45, 56]. To reduce the impact of the boundary resistance, liquid helium cells commonly use sintered metal-powder as heat exchangers [16, 57], benefiting from the large relative surface area of sintered powder [58].

Helium-3 immersion has been successful in cooling two-dimensional electron gases to 0.9 ± 0.1 mK [59] and immersion in ^{3}He – ^{4}He mixture has cooled electrons in a CBT

to 3.7 mK [21]. Liquid helium is commonly used as a heat exchanger in immersion cooling and does not produce cooling power. As such, immersion cooling is limited by the boundary resistances between liquid helium, experiment and refrigerant. The notable exception is immersion in helium mixture where cooling power is produced by and limited in temperature by dilution refrigeration. Using this technique often requires modifications to a dilution refrigerator to install a liquid helium experimental cell [60] or install an experiment inside the refrigerator's mixing chamber [21].

2.3.2 Thermoelectric cooling.

Thermoelectric coolers and effects were discovered by and Peltier and Seebeck who discovered that applying a voltage across a junction between two different materials could also create a temperature separation across the junction [61]. The reverse is also true where a temperature difference across a junction can induce an electromotive potential. The induced temperature difference and cooling power of thermoelectric junctions strongly depends on the material properties of either side. With a careful choice material, this effect can be used to create heat pumps optimised for particular temperatures and cooling powers [62]. The potential for thermoelectric coolers to integrated into circuitry and cool electrons on-chip make them a system of great interest for nanoelectronics and quantum devices [63].

Peltier refrigerators have been widely used in physics to cool down to 100 K with weakening efficiency at lower temperatures [14]. It has been proposed that the weak thermal conductivity and specific heat at millikelvin temperatures could be exploited for millikelvin thermoelectric cooling [64]. At this temperature range, there is also the possibly to use the inherent properties of metal-insulator transition materials to cool below liquid helium temperatures [65].

Recent research developments have focused on junctions between superconductors

and normal or insulating materials [66]. Electronic coolers of this style use a material energy gap as a filter to selectively remove high energy electrons from one side of the junction. This coling method is not limited to superconductors, a similar approach using quantum dots as energy filters has been used to cool two-dimensional electron gases [67]. Energy gap coolers of this type can suffer from a narrow operational temperature range since the energy filters cannot be tuned. Superconductor-quantum dot hybrid coolers have been proposed to solve the narrow operational band [68]. These energy filters created by bandgap engineering can also be used as thermometers where instead of focusing on removing them, the population of high energy can be measured and used to infer temperature on one side of the junction [69].

Thermoelectric coolers have great potential for on-chip cooling to below 100 mK [70]. They are limited in use by narrow operational temperatures, difficulties of fabricating superconducting gaps and a freezing of charge carriers at the lowest temperatures [66]. Phonon thermal conduction lowers the efficiency of junction coolers, overwhelming cooling power at low temperatures without significant efforts to limit phonon transport [71]. Designing a thermoelectric refrigerator to cool electronic systems into the microkelvin regime would require significant exploratory efforts, investigating gap engineering, materials and thermal isolation.

2.4 Coulomb blockade thermometry

Consider an isolated finite metallic volume flanked on one side by a thin insulating barrier that is itself connected to an infinite metallic volume. With a sufficiently thin barrier, electrons can tunnel onto and away from this central ”island” volume. An electron tunnelling onto the island will add to the total charge of this island and must have enough energy to both traverse the insulating barrier and overcome the electrostatic repulsion of the charged island. The island will have a capacitance relative

to the nearby metallic volume. We can define a charging energy of E_C which represents the minimum electron energy required to add one electron to the island.

$$\mathrm{E}_C = \frac{1}{2}\frac{e^2}{C_{\mathrm{total}}} \tag{2.23}$$

where e is the electron charge and C_{total} is the total capacitance of the island. At low temperature the thermal energy of electrons in the metallic volumes is described by $k_{\mathrm{B}}T_e$. If this energy is much less than the island charging energy, there will be no conductance of electrons across the barrier, a state called total coulomb blockade. If the thermal energy is much greater than the charging energy, electrons will freely tunnel onto and off the island, though limited by an effective tunnelling resistance determined by the construction and geometry of the junction. When the thermal energy is close to the charging energy there will be a finite conductance, the value of which is strongly dependant on the temperature of the electron bath. This means that for an island with a defined and fixed capacitance tuned such that it is close to total Coulomb blockade, a measurement of conductance can be used to calculate an electron temperature.

An electron hopping on to the island adds its charge to that island, leading to an increase in island capacitance and required charging energy for the next electron, affecting any measurement of conductance. To minimise the impact of individual electrons and random offset charges, Coulomb blockade thermometers (CBTs) are made from chains of many tunnel junctions and islands with multiple chains in parallel. An schematic of one such tunnel junction can be found in figure 2.4 along with an image of a CBT used in this study. The CBTs used and investigated in this work are made with 33 tunnel junctions in a chain (34 islands flanking them) with 20 chains in parallel. The individual conductances of each junction combine to a total effective conductance across the whole array.

2.4.1 Measuring temperature with a Coulomb blockade thermometer

Temperature measurements with a CBT are performed by applying a voltage bias across the tunnel junction array. Depending on sign and magnitude, this voltage bias will lower or increase the required electron energy to charge an island, changing total conductance. At a high bias, the conductance will saturate at a value determined by the effective tunnelling resistance. In a CBT the capacitance is tuned to a fixed value so that the array approaches total Coulomb blockade for a desired range of electron temperatures. As the voltage bias is swept towards zero bias the conductance will decrease to a minimum at zero volts, where conductance is then determined by electron temperature. The minimum conductance reach and the rate at which conductance falls to a minimum both depend on electron temperature. Examples of bias sweep conductance measurements are given in figure 2.3. The temperature can be extracted by measuring by fitting a master equation model or a Markov chain Monte Carlo model to the full bias-sweep conductance curve. The description and derivation of these models go beyond the scope of this work but are described in [28]. Alternatively, the width of the conductance curve halfway to the minimum conductance (FWHM) is given by

$$\mathrm{FWHM} = 2 \times G \frac{k_\mathrm{B} T_e}{e}. \tag{2.24}$$

where G is a unitless constant determined by the construction and the inbuilt island capacitance of the CBT. For the CBT used in this study, G is 5.127. The derivation of this relation also goes beyond the scope of this work and is described in [44, 51, 55]. When using a FWHM measurement the CBT can be considered a primary thermometer for electron temperature as the FWHM depends on no fitting parameters or other

empirically derived constants. It depends only on electron temperature. The working range of a CBT is limited in electron temperature. As electron temperature decreases and the thermometer approaches total Coulomb blockade, the conductance curve narrows and the zero bias dips to a lower conductance. At high electron temperatures, the curve broadens and dip lessens. At sufficiently low temperature total Coulomb blockade is achieved, conductance curve fitting and FWHM measurement are no longer applicable. At a sufficiently high temperature the conductance curve is too broad and the dip to shallow to be measured, indistinguishable from the high-bias conductance. The capacitance of a CBT must be carefully tuned to decide which range of electron temperatures it will be sensitive to.

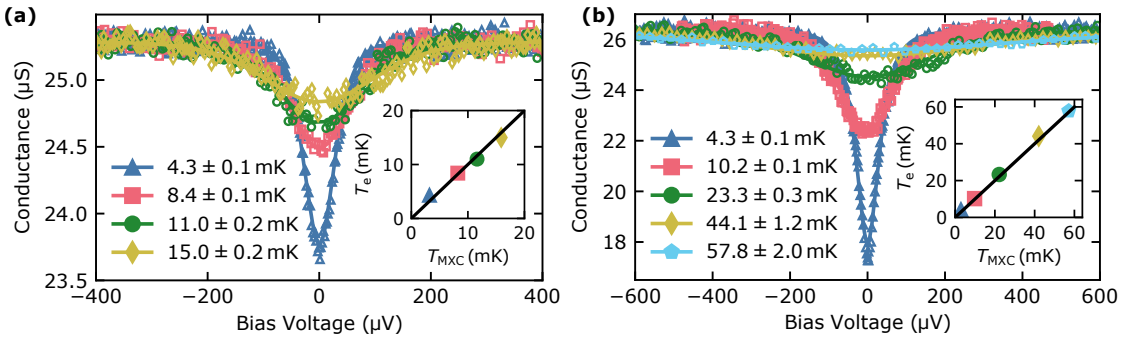

Figure 2.3: Voltage bias conductance measurements on a common-gate capacitance CBT (left) and junction-capacitance CBT (right). These measurements do not use demagnetisation cooling, instead the thermometers are thermalised with a mixing chamber which is held at a number of fixed temperatures. The electron temperatures are extracted by fitting the full conductance curve and the insets show how these fitted temperatures compare to measured mixing chamber temperatures. Plots were generated by the author using data gathered by A. Jones and J.R. Prance. This data can also be found in [1, 22, 28, 55].

2.4.2 Cooling a Coulomb blockade thermometer

Coulomb blockade thermometers are highly sensitive to the temperature of electrons which travel through their tunnel junction array, making them ideal for testing methods of directly cooling electrons. As highly resistive devices, electrons internal to a CBT are thermally isolated from hotter measurement wires and the host experimental environment. Previous studies of electron refrigeration made use of this isolation by placing exposed metallic blocks, electrically connected to the CBT circuitry, between the CBT's tunnel junctions and immersing these blocks in helium mixture [21]. More recent studies have replaced these thermalisation blocks with magnetic refrigerant, creating volumes of cold electrons in direct contact with CBT circuitry [1, 22, 26, 28, 44]. An example of this structure, the effective unit cell of the CBT, is shown in figure 2.4 along with an image of a CBT with copper refrigerant.

It is difficult to directly compare and evaluate the performance of on-chip demagnetisation refrigeration in these studies. The studies make use of different refrigerant materials and geometries as well as off-chip demagnetisation of the measurement wiring and experimental environment. All of this is further obfuscated by the dynamics of CBTs at microkelvin temperatures, which are themselves a worthy subject of study. The work in this thesis models and investigates the Lancaster on-chip demagnetisation experiments [1, 22, 24, 28, 55] where no off-chip demagnetisation cooling was used. The only source of refrigeration below helium dilution was the on-chip magnetic refrigerant. This set of experiments are the best candidates for modelling and evaluating the cooling power of on-chip refrigeration alone.

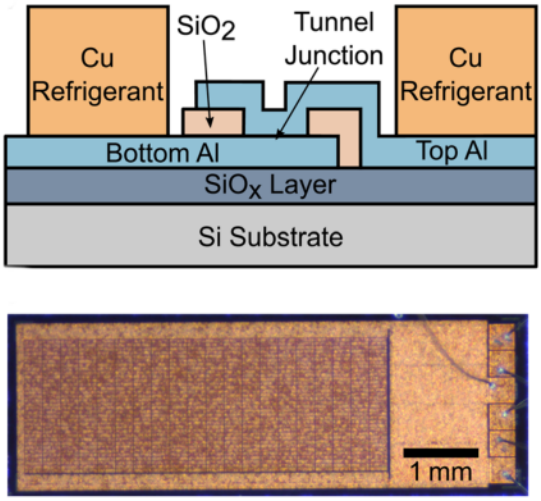

Figure 2.4: A representation of one 'unit cell' of a junction CBT showing a tunnel junction flanked by two islands of copper nuclear refrigerant. Below this schematic is a microscope image of the actual thermometer with the grid pattern on the left showing the 20 chains of 33 tunnel junctions. The schematic and image were made by and used with the permission of A. Jones, also found in [22, 55].

Chapter 3

Simulating On-chip Demagnetisation

This chapter describes simulating demagnetisation cooling and thermal evolution of the non-linear thermal systems within on-chip nuclear refrigerant at millikelvlin temperatures. The chapter starts with section 3.1 where it describes the construction of the simulation based on the thermal model from subsection 2.2.1. In section 3.3 results of the simulation are compared to on-chip cooling experiments.

3.1 Simulating on-chip demagnetisation

On-chip demagnetisation cooling has succeeded in cooling coulomb blockade thermometers to microkelvin temperatures but always in conjunction with other cooling techniques. Previous experiments have revealed a need for further understanding the power and potential of on-chip cooling as discussed in subsection 2.2.2. A simulation of on-chip cooling will allow for the refrigeration and thermalisation of this technique to be explored.

3.1.1 Temperature evolution

On-chip demagnetisation cooling evolves in time, temperature, and magnetic field. This evolution is highly nonlinear so in simulation there must be careful consideration of limits and choice of method. This work assumes that the involved thermal systems evolve quasi-statically and are well thermalised with each other. This assumption allows for nuclear spin temperature to be described adiabatically as a function of magnetic field.

A thermal model of on-chip cooling is described in subsection 2.2.1 and shown in Figure 2.2. This model identifies three thermal systems internal to the island: magnetic nuclear spins, conduction electrons and phonons. A heatflow schematic is shown in Figure 3.1 The temperature evolution $\dot{T}$ of each system with heat capacity C can be described by the summation of heat flowing into $\dot{Q}_{\text{in}}$ and out $\dot{Q}_{\text{out}}$ of the system. To obey the quasi-static assumption, this must be evaluated only over small time-steps *dt*. As a general description:

$$\dot{T} = \frac{\dot{Q}_{\text{in}} - \dot{Q}_{\text{out}}}{C}. \tag{3.1}$$

For the nuclear magnetic spins, the thermal model identifies only one thermal link, the hyperfine interaction between electrons and nuclei. Conduction electrons are continually heated by a parasitic heat leak $\dot{Q}_{\text{leak}}$ which we assume to be a constant fixed power. The electrons share heat with internal phonons via electron-phonon coupling. The internal phonons with temperature T_{p} are thermally linked to external environment phonons via an effective Kapitza resistance between the nuclear refrigerant and a silver strip. The phonon temperature of the silver strip is assumed to be equal to the mixing chamber temperature $T_{\text{p,Ag}} = T_{\text{MXC}}$ and with a temperature independent of on-chip cooling. The thermal evolution of internal island temperatures can then be defined by

a system of differential equations:

$$\dot{T}_\mathrm{n} = \frac{\dot{Q}_\mathrm{en}}{C_\mathrm{n}} \tag{3.2}$$

$$\dot{T}_\mathrm{e} = \frac{\dot{Q}_\mathrm{pe} - \dot{Q}_\mathrm{en} + \dot{Q}_\mathrm{leak}}{C_\mathrm{e}} \tag{3.3}$$

$$\dot{T}_\mathrm{p} = \frac{\dot{Q}_\mathrm{pp} - \dot{Q}_\mathrm{pe}}{C_\mathrm{p}}. \tag{3.4}$$

The heat-flows in set of equations are defined in subsections 2.1.3 and 2.1.4 and are restated here for convenience. Heat-flow from electrons to nuclear spins is given by

$$\dot{Q}_\mathrm{en} = C_\mathrm{n}\frac{dT_\mathrm{n}}{dt} = \frac{C_\mathrm{n}}{\kappa}\left(T_\mathrm{e} - T_\mathrm{n}\right)T_\mathrm{n} = \frac{\lambda n}{\mu_0 \kappa}\frac{\left(B^2 + b^2\right)}{T_\mathrm{n}}\left(T_\mathrm{e} - T_\mathrm{n}\right), \tag{3.5}$$

heat flowing from phonons to electrons is

$$\dot{Q}_\mathrm{pe} = \Sigma V\left(T_\mathrm{p}^q - T_\mathrm{e}^q\right) \tag{3.6}$$

and the phononic heat flow across a boundary between two different materials (from material x to y) is approximated by

$$\dot{Q}_\mathrm{xy} = \left(T_\mathrm{x} - T_\mathrm{y}\right)/R_\mathrm{K} = \left(T_\mathrm{x} + T_\mathrm{y}\right)^2\left(T_\mathrm{x}^2 - T_\mathrm{y}^2\right)\frac{A}{8r_\mathrm{K}}. \tag{3.7}$$

In this specific model, we use $\dot{Q}_\mathrm{pp}$ to refer to the boundary heat-flow and it is always defined as a flow from the experimental environment and via the silver strip with temperature $T_\mathrm{p,Ag}$ towards the phonons inside the nuclear refrigerant with temperature T_p.

Electron-nuclear heat flow can be calculated using equation (3.5). Equation (3.6) describes electron-phonon heat flow and equation (3.7) can be used to find the phononic

boundary heat flow. Nuclear heat capacity is given by equation (2.12), restated here:

$$C_{\mathrm{n}} = \frac{n\lambda_{\mathrm{n}}B^2}{\mu_0 T^2}. \tag{3.8}$$

The conduction electron heat capacity is [24]

$$C_{\mathrm{e}} = \frac{\pi^2}{2} nR \frac{T_{\mathrm{e}}}{T_{\mathrm{F}}} \tag{3.9}$$

where n is the number of moles, R the ideal gas constant and T_{F} the Fermi temperature. The phonon heat capacity is given by [16]

$$C_{\mathrm{p}} = \frac{12}{5}\pi^4 nR \left(\frac{T_{\mathrm{p}}}{\Theta_{\mathrm{D}}}\right) \tag{3.10}$$

where Θ_{D} is the Debye temperature. With all heat flows and heat capacities calculable, the system of differential can then be numerically integrated to simulate on-chip demagnetisation cooling.

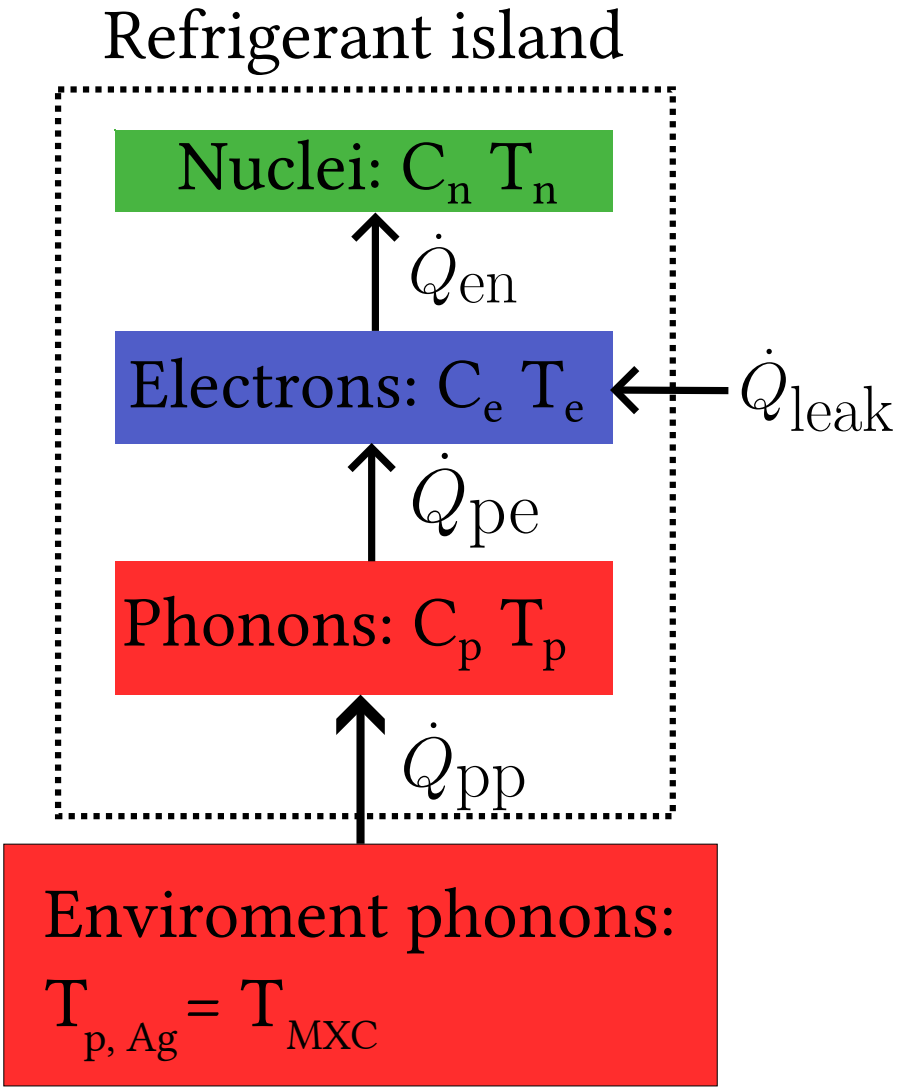

Figure 3.1: A schematic of the thermal heatflows involved in on-chip demagnetisation. A block of copper contains three different thermal systems with their own heat capacities and temperatures: conduction electrons *e*, magnetic nuclear spins *n* and phonons *p*. Electron-nuclear heat flow is given by $\dot{Q}_{en}$. Similarly, heat flow from refrigerant phonons to electrons is given by $\dot{Q}_{pe}$. The refrigerant is separated from experimental environment phones which are well thermalised with a dilution refrigerator with mixing chamber temperature T_{MXC}. There is a heatflow from the external phonons to refrigerant phonons given by $\dot{Q}_{pp}$. The electron system is heated by an external heat leak $\dot{Q}_{leak}$ which is assumed to have a fixed power.

3.1.2 Numerical integration

As shown in subsection 2.1.1, the ideal adiabatic cooling of a nuclear magnetic spins evolves with applied magnetic field. A finite step in magnetic field produces a finite step in nuclear temperature and B/T_n is constant. We can then define a step-wise process for a simulation.

1. Step the magnetic field by some finite value.

2. Calculate the new nuclear spin temperature at the new field strength.

3. Allow the thermal systems to evolve over a number of equilibration steps.

4. Use the final equilibration temperatures as the starting temperatures for the next field step calculation.

5. Repeat from step one.

The simulation in this work is written in Python using the SciPy integrate function, odeint [72]. This function uses the lsoda algorithm [73] to integrate systems of ordinary differential equations with a known starting value. The simulation is given the starting temperature of all systems along with the field profile and measured mixing chamber temperatures if not constant through demagnetisation. Following the step-wise process defined above, the simulation steps the magnetic field every second. This field step is used to calculate a new magnetic nuclear spin temperature by equation (2.14). The thermal systems are then solved for one hundred equilibration steps adding up to one second and the resultant temperatures are used as the starting point for the next step in field. The code for this simulation is available on request.

3.1.3 Simulation parameters

The necessary material parameters, upon which the simulation runs, are summarised in Table 2.1. These parameters are derived from book values or measurements for each material. Not included in this list are the total Kapitza resistance and the experimental heat leak which are specific to experimental setup. Figure 3.2 shows measured temperatures during pre-cooling of a Lancaster gate-CBT (gCBT), a CBT where junction capacitance can be controlled by a common top gate [28]. The simulation is given a steady 8 T field and the measured mixing chamber as silver phonon temperature. The measured electron temperature at −300 ks is used as the starting temperature for the simulated island electron, phonon and nuclear systems. During pre-cooling, the coldest system in the thermal model is the silver phonons and the only significant temperature difference is between the silver and copper phonons. Heat internal to the island must be cooled through the island-silver phonon boundary and thus must be most sensitive to the Kapitza resistance. Fitting the simulation to the early section of pre-cooling where the heat leak is negligible yields $R_{\mathrm{pp}} = 0.8 \times 10^{-2}\,\mathrm{K^4 m^2/W}$. The experimental heat leak becomes more important in the later part of pre-cooling, close to $t = 0$, where there internal temperatures have a notable separation. Varying the heat leak parameter in simulating this later pre-cooling gives a heat leak of $Q_0 = 0.1\,\mathrm{fW}$. Similar pre-cooling fitting with a Lancaster junction-CBT (jCBT) yields $R_{\mathrm{pp}} = 1.5 \times 10^{-2}\,\mathrm{K^4 m^2/W}$. In this type of CBT the junction capacitance is dominated by nearest-neighbour coupling [55].

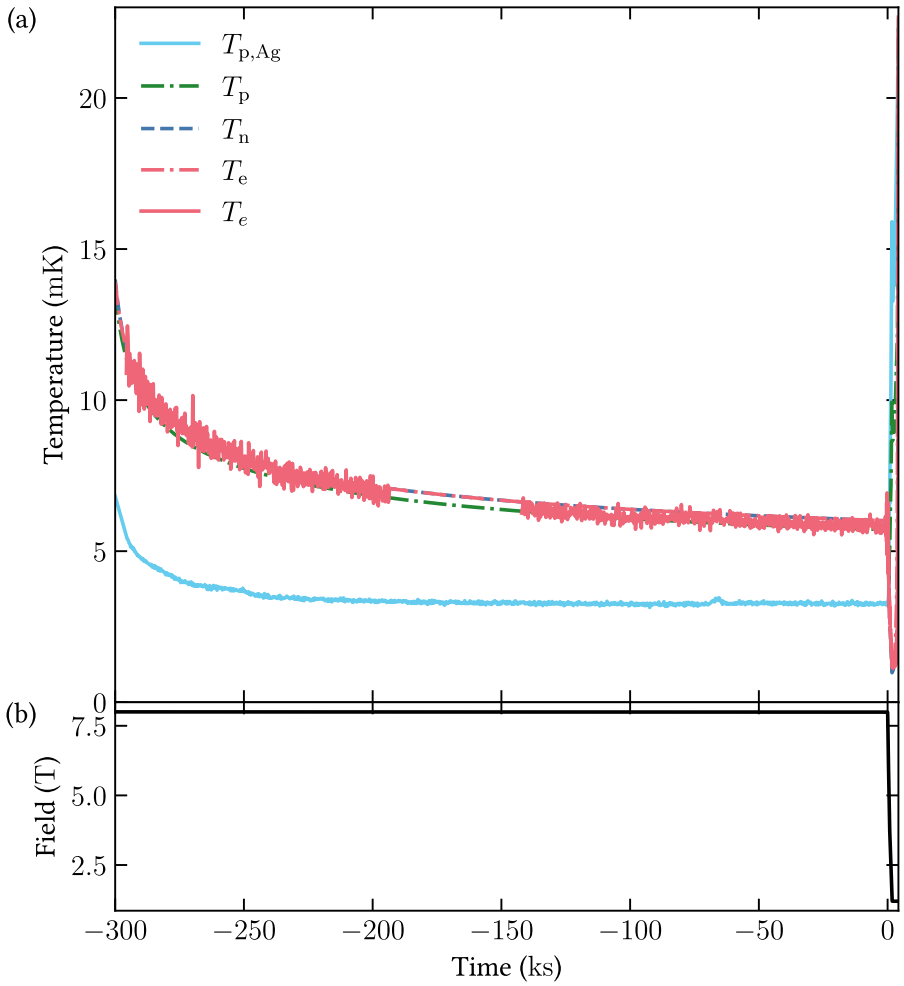

Figure 3.2: Measured and simulated temperatures of a pre-cooling gCBT. The solid lines show the measured electron temperature T_e and silver phonon temperature $T_{p,Ag}$. Segments of the measured electron temperature are removed to highlight the simulated (dash-dot) temperatures. The simulated temperatures are given the initial conditions and silver phonon temperature of the real device and then allowed to evolve independently. The simulation fitting parameters are a total Kapitza resistance of $0.8 \times 10^{-2}\,\mathrm{K^4m^2/W}$ and a constant 0.1 fW heat leak into the electrons.

3.2 Comparisons between simulation and CBT experiments

The simulation is based only on theory-derived and experimentally-measured parameters and constants. While this may give some expectation that the results are physically accurate, comparing the simulation results to experimental data will allow for this accuracy to be formally evaluated and give confidence to derived conclusions and results. The experimental data used here is temperature data from two different types of coulomb blockade thermometer (CBT) which are pre-cooled in a custom Lancaster wet dilution refrigerator. The construction of the thermometers is described in Jones [55] and Autti [1], the latter also giving us the relevant parameters on which to run the simulation. Each CBT has an array of 32×20 islands separated by tunnel junctions. The islands are $205\,\mu m \times 6.5\,\mu m \times 39\,\mu m$ blocks of electroplated copper. Replicating the dynamics of tunnel junction arrays is beyond the scope of this work so only the temperature evolution of one island will be simulated, ignoring nearest-neighbour or chain effects.

3.3 Comparing demagnetisation experiments and simulation

Figure 3.3 shows simulated temperatures alongside measured temperatures in a junction-CBT demagnetisation experiment. The Kapitza resistance and constant heat leak are extracted from pre-cooling measurements of the j-CBT. The starting simulated island temperatures are set to the measured electron temperature. The simulation is also given the magnetic field profile and the mixing chamber temperature as silver phonon temperature.

Throughout pre-cooling and the start of demagnetisation, the simulated and measured temperatures are in near perfect agreement. Simulation and measurements start to diverge at 1500 s, the measured electron temperature reaching a plateau at 1.0 ± 0.1 mK whereas the simulated electron temperature cools down to ≈340 µK. This limit in measured temperature is likely due to saturation of the readout known for this type of thermometer [1] so it likely that this thermometer did cool down to microkelvin temperatures. During and after demagnetisation the mixing chamber heats up due to eddy current heating of the refrigerator structure appearing in the mixing chamber after some delay. Despite this non-ideal refrigerator warming the simulation captures the warm-up behaviour and hold time of the jCBT.

Figure 3.4 shows temperatures measured in a demagnetisation experiment using a gate-CBT. This type of CBT features a top gate which provides another thermal route for phonon heat conduction. This thermal link is not modelled by the simulation but is taken into account by a lower effective total Kapitza resistance of $R_{\mathrm{pp}} = 0.8 \times 10^{-2}\,\mathrm{K^4m^2/W}$. The simulation starting temperatures, field profile, constant heat leak and $T_{\mathrm{p,Ag}}$ are taken from experimental data. The cooling and lowest temperature of electrons in this experiment are well-captured by the simulation down to the lowest electron temperature, including warm up and a hold time to within 200 seconds.

The simulation makes no attempt to model Coulomb blockade thermometer operation nor dynamics. Regardless, electron temperatures in CBTs with on-chip cooling are well described by the first-principles simulation and thermal model of one cooling island. The close agreement between experiments and simulations for abnormal mixing chamber behaviour and both types of CBT is evidence for this. It is difficult to discern the cooling capacities of on-chip refrigerant for both thermometers and predict their final temperatures and hold times. With a simulation that accurately models experimental behaviour, the limits, constraints and performance of on-chip

cooling can be predicted and explored.

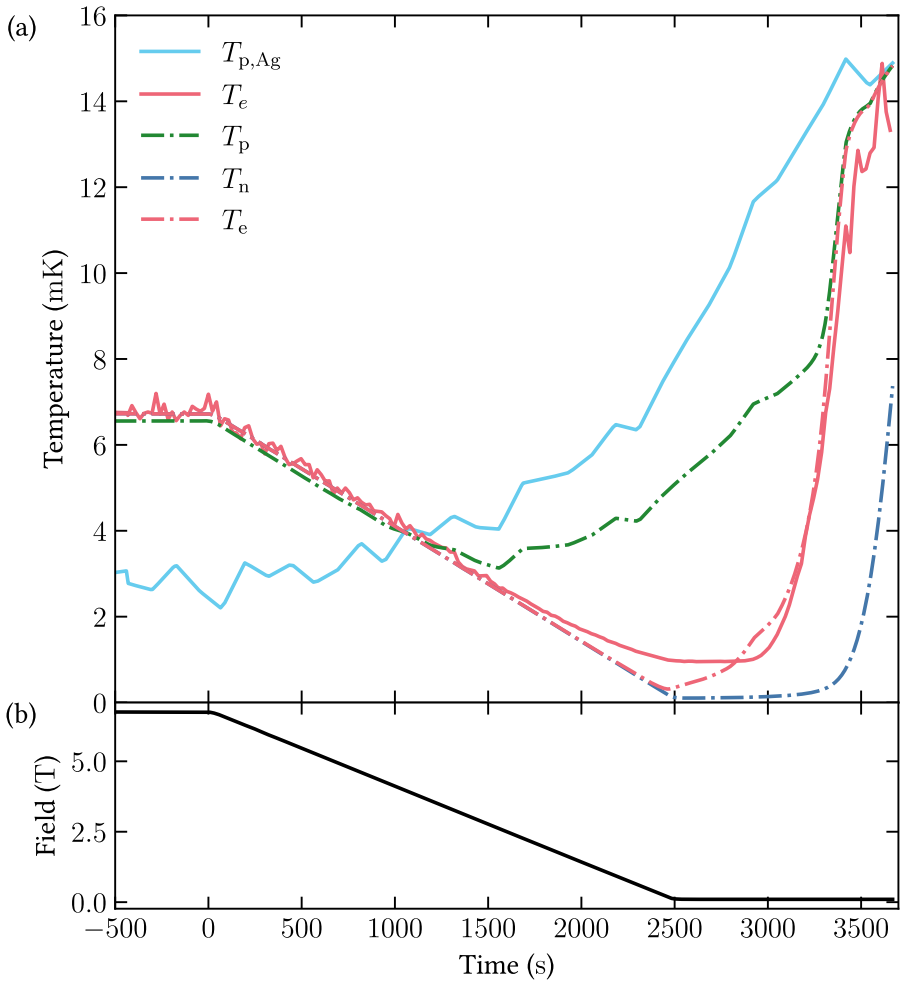

Figure 3.3: Simulated and measured temperatures in a jCBT demagnetisation experiment. (A) The measured temperatures are shown by solid lines for electrons (salmon) and mixing chamber temperature $T_{p,Ag}$ (cyan). The simulation begins at −200 ks with phonon T_p, electron T_e and nuclear T_n starting temperatures set equal to the measured electron temperature. The simulation is given the field profile and $T_{p,Ag}$ as measured in the experiment. Simulated temperature are shown by the dash-dot lines. The fitted Kaptiza resistance $R_{pp} = 1.5 \times 10^{-2}\,K^4m^2/W$ and constant heat leak of $Q_0 = 0.1\,fW$ are derived from pre-cooling of the j-CBT. (B) The magnetic field is set to 6.75 T during pre-cooling. Demagnetisation begins at $t = 0$ and the field decreases linearly to 100 mT over 2.5 ks.

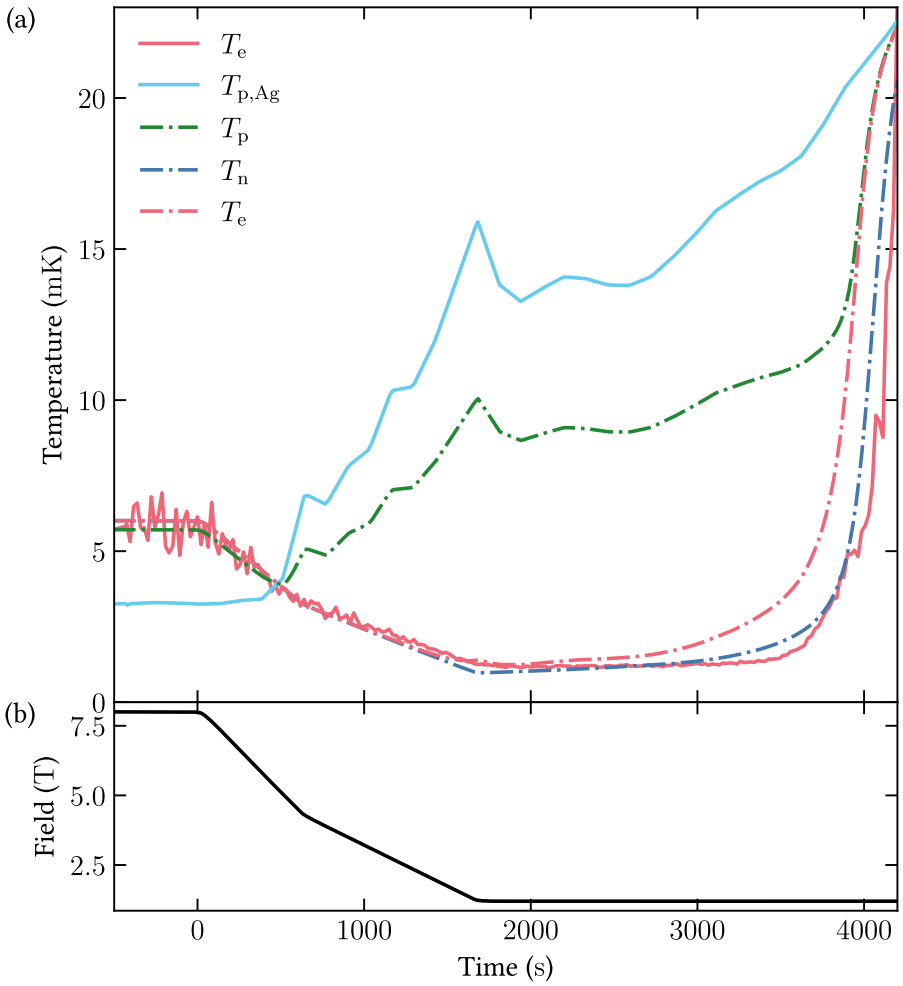

Figure 3.4: Simulated (dot-dashed) and measured (solid) temperatures in a gCBT demagnetisation experiment. The simulation beings at −300 s with initial nuclear, phonon and electron temperatures set equal to the measured T_e. The measured mixing chamber of the refrigerator is assumed to be equal to the silver phonon temperature $T_{p,Ag}$ and the simulation progresses under the same field profile as the experiment. The measured and simulated electron temperatures both cool to ≈1.1 mK. The increasing phonon temperature and associated phonon-electron heat leak eventually overwhelms the cooling capacity of nuclear spins leading to the rapid warming of the simulation and experiment. (B) At time $t = 0$ the magnetic field sweeps from 8 T to 1.2 T over 1600 s and is held constant for the remaining duration.

Chapter 4

Simulation parameter search

This chapter uses the simulation built in chapter 3 to explore the limits, constraints and optimisation of on-chip demagnetisation cooling (OCDC). The sections are organised to narrow down the possible changes to sample and sample environment to not only optimise on-chip cooling but suggest how it may be best integrated into low temperature experiments and what the key parameters or figures are.

4.1 Simulation Setup

A standard nomenclature and colouring, consistent with the thermal model in Figure 2.2 is used in this chapter to refer to different heat flows and thermal subsystems. The temperature of a subsystem internal to one demagnetisation island is represented by T_x, where x denotes electrons e, nuclear spin n and phonon temperature p. Similarly, $\dot{Q}_{\mathrm{x,y}}$ represents the instantaneous heat flow power from subsystem x to y. The phonon temperature of a silver chip-carrier, assumed to be in strong thermal contact with a mixing chamber, is represented by $T_{\mathrm{p,Ag}}$ which is the thermalisation and cold point of the system. This phonon temperature is linked to the internal phonons via a Kapitza resistance. Lastly, $\dot{Q}_{\mathrm{leak}}$ is a fixed-power heat leak based on experimentally-observed

powers which heats the electron bath internal to the demagnetisation island. For more detail on the thermal subsystems, see Figure 2.2 and subsection 2.2.1.

The starting parameters for exploring the simulation are based on the measured parameters from the Lancaster jCBT experiments: the Kapitza resistance is set to an R_{pp} of $1.5 \times 10^{-2}\,\mathrm{K^4 m^2/W}$, the electronic heat leak $\dot{Q}_{\mathrm{leak}}$ is 0.1 fW and the magnetic field sweeps from 6.75 T to 100 mT over 2500 s. Instead of using the variable fridge temperature of the jCBT experiment, performed in a bespoke Lancaster wet dilution refrigerator, the parameter-search instead starts with an ideal 10 mK base fridge temperature to represent the base temperatures of commonly-available commercial dilution refrigerators with an added magnet for demagnetisation. These parameters are used in all simulations within this Chapter unless explicitly stated otherwise.

Refrigeration with this on-chip demagnetisation technique is highly sensitive to refrigerator temperature [1] yet outside of Lancaster this technique has cooled electrons to below 500 µK in refrigerators with higher base temperatures [27, 28]. As such, refrigerator temperature alone cannot explain the variance temperatures between experiments in Lancaster [1, 55] nor in other institutions [27, 28]. With a simulation of this cooling technique, the parameter-space can be explored to resolve this difference and find the best conditions for enabling and optimising on-chip demagnetisation cooling.

This search begins with changing the experiment environment and external influences which affect on-chip cooling. Firstly, section 4.2 explores the difference between on-chip demagnetisation in a standard commercial 10 mK dilution refrigerator and a bespoke 3 mK refrigerator. section 4.3 details the effects of changing the applied magnetic field strength and the demagnetisation sweep profile. section 4.4 investigates the importance of controlling heat leaks and to which degree they must be minimised. Next the parameter-search looks to internal device factors. In section 4.5

the construction of the device is modified to vary phonon heat flow between it and the host refrigerator. Lastly, section 4.6 investigates how changing the on-chip refrigerant itself influences demagnetisation cooling performance.

4.2 Effect of fridge temperature

Changing the environment or sample temperature affects nearly every part of demagnetisation refrigeration. The heat flow between the cooled nuclear spin system and device electrons is given by

$$\dot{Q}_{\mathrm{en}} = \frac{\lambda n}{\mu_0 \kappa} \frac{\left(B^2 + b^2\right)}{T_{\mathrm{n}}} \left(T_{\mathrm{e}} - T_{\mathrm{n}}\right) = \frac{C_{\mathrm{n}}}{\kappa} \left(T_{\mathrm{e}} - T_{\mathrm{n}}\right) T_{\mathrm{n}} \tag{4.1}$$

and scales with $T_{\mathrm{e}} - T_{\mathrm{n}}$ for $T_{\mathrm{e}} \;\; T_{\mathrm{n}}$ and $1/T_{\mathrm{n}}$ for $T_{\mathrm{e}} \gg T_{\mathrm{n}}$ but with no change in coupling strength when both temperatures are increased or decreased by the same factor. The heating of the electron system via the demagnetisation island phonons, given by

$$\dot{Q}_{\mathrm{pe}} = \Sigma V \left(T_{\mathrm{p}}^5 - T_{\mathrm{e}}^5\right) \tag{4.2}$$

and scales with the difference in temperatures $T_{\mathrm{p}}^5 - T_{\mathrm{e}}^5$ when $T_{\mathrm{p}} \;\; T_{\mathrm{e}}$ and with T_{p}^5 for $T_{\mathrm{p}} \gg T_{\mathrm{e}}$. Both equations are derived and discussed in subsection 2.1.1. With a fall in temperature, the phonon-electron coupling will weaken but the electron-nuclear coupling will stay roughly constant for the same proportional difference between subsystem temperatures. With electron-phonon coupling falling at a faster rate than electron-nuclear, there is a crossover point where electron-phonon heat flow becomes weaker than electron-nuclear heat flow. Electron cooling after this point is then dominated by nuclear cooling capacity. Reaching this crossover as early as possible will maximise the refrigeration potential of demagnetisation cooling.

Figure 4.1 shows the simulated electron temperatures of two copper islands under demagnetisation in 3 and 10 mK refrigerators. Both electron systems start well thermalised with their respective refrigerators and steadily cool during demagnetisation. The 10 mK system's electrons feature a point of inflection around 2.4 ks before the end of demagnetisation. The electrons then rapidly warm and reach equilibrium with the dilution refrigerator. The 3 mK does not show this sudden switch between cooling and warming and remains cold for significantly longer with slower rates of warming. Not shown on the scale of this figure is that the electron bath continues to warm but does not reach parity with the 3 mK refrigerator temperature before the simulation ends at 16 ks. The offset in final electron temperature from the fridge temperature is due to the significantly smaller nuclear heat capacity at low magnetic field [nuclear spin heat capacity scales with B^2 see Equation 2.12] such that the constant 0.1 fW heat leak creates an equilibrium point marginally above refrigerator temperature for the electron and nuclear systems.

These electron-temperature traces behave differently in 3 and 10 mK refrigerators. The 10 mK refrigerator simulation features an inflection point in electron temperature and warms up before demagnetisation has completed whereas 3 mK refrigerator simulation does not. It is not immediately obvious how refrigerator temperatures produce this difference in behaviour. Figure 4.2 shows the internal phonon and nuclear spin temperatures as well as the internal heat-flow for the same simulations. For the 3 mK refrigerator simulation, the electro-nuclear heat-flow is ten times stronger than the electron-phonon heat flow [0.109 fW versus 0.009 fW] with heating in this situation dominated by the 0.1 fW electronic heat-leak, Q_{leak}. It is decoupling which allows the electro-nuclear system to be largely independent of internal phonon temperature and thus refrigerator environment temperature. As a result the electrons have a long hold-time below 1 mK. In the 10 mK refrigerator simulation, the phonon coupling with the

electron bath is stronger due to its T^5 dependence, resulting in heat flows on the order of ~1.5 fW. For the electron bath to flip from cooling to warming, as is seen in the 10 mK demagnetisation, the expectation is to observe a notable crossover point where electro-nuclear cooling is smaller in magnitude than the phonon heating and heat leak contributions together. At the point where electrons start to warm, there does not seem to be a change in heat flow magnitude between the thermal systems on this figure.

The general trend of $\dot{Q}_{\mathrm{en}}$ and $\dot{Q}_{\mathrm{pe}}$ is to increase in strength as the system temperatures diverge acting akin to a restoring force pushing the system back to equilibrium. The difference between them is that $\dot{Q}_{\mathrm{pe}}$ trends to a maximum of $\Sigma V T_{\mathrm{p}}^5$ for $T_{\mathrm{e}} \ll T_{\mathrm{p}}$ whereas $\dot{Q}_{\mathrm{en}}$ does not trend to a maximum. Electron-nuclear heat flow, when $T_{\mathrm{n}} \ll T_{\mathrm{ep}}$, continues to increase with falling nuclear temperature due to the $1/T_{\mathrm{n}}$ term in (4.1). This difference in behaviour at diverging temperatures is what allows the system to cool and keep cooling much below T_{p} provided $\dot{Q}_{\mathrm{en}} > \dot{Q}_{\mathrm{pe}}$ in the absence of any heat leak. Effective cooling therefore requires controlling the balance between these heat flow powers and finding under which conditions one might overwhelm the other.

To understand more about the balance and the crossover point, the heat flow powers are calculated for a range of temperatures to find under which conditions the electron-phonon heating and electro-nuclear cooling match. The calculation is performed by setting

$$\dot{Q}_{\mathrm{en}} = \dot{Q}_{\mathrm{pe}}. \tag{4.3}$$

Equations (4.1) and (4.2) can then be rearranged to give

$$T_{\mathrm{p}} = \left(\frac{n\lambda}{\Sigma V \mu_0 \kappa} \frac{B^2 + b^2}{T_{\mathrm{n}}} (T_{\mathrm{e}} - T_{\mathrm{n}}) + T_{\mathrm{e}}^5 \right)^{1/5} \tag{4.4}$$

which, for a constant electron temperature, can then be graphed to show lines of equal heat flow power. This expression is only valid for $T_n < T_e < T_p$ to avoid imaginary roots and maintain a defined direction of heat-flow and this limit should always hold true during demagnetisation.

Figure 4.3 shows these curves of equal heat-flow power for multiple electron temperatures. If a sample of copper has an electron, phonon and nuclear spin temperature such that it sits one one of the equal-power lines, the electron temperature will remain steady for as long as the nuclear spin heat capacity is not exhausted. If instead the system has electron temperature above or below the equilibrium lines, the electrons will warm or cool respectively to reach equilibrium.

The equilibrium lines show a strong field-dependence which shifts them upwards in phonon temperature. This is due the B^2 term in equation (4.1) increasing heat flow with increasing field strength. A stronger field induces a higher nuclear spin heat capacity and stronger electro-nuclear coupling. As nuclear spin temperature approaches electron temperature, the electron-nuclear cooling linearly approaches zero due to a $T_e - T_n$ term in Equation (4.1) causing Equation (4.4) to fall to a minimum. This crossover is also the point where the difference between phonon and electron temperature becomes so great that $\dot{Q}_{pe}$ effectively becomes a constant for constant T_p. It is here, roughly at a phonon temperature of 3 mK, where the equilibrium lines become vertical and the system will always cool provided $T_n < T_e$ and T_p does not warm above three millikelvin.

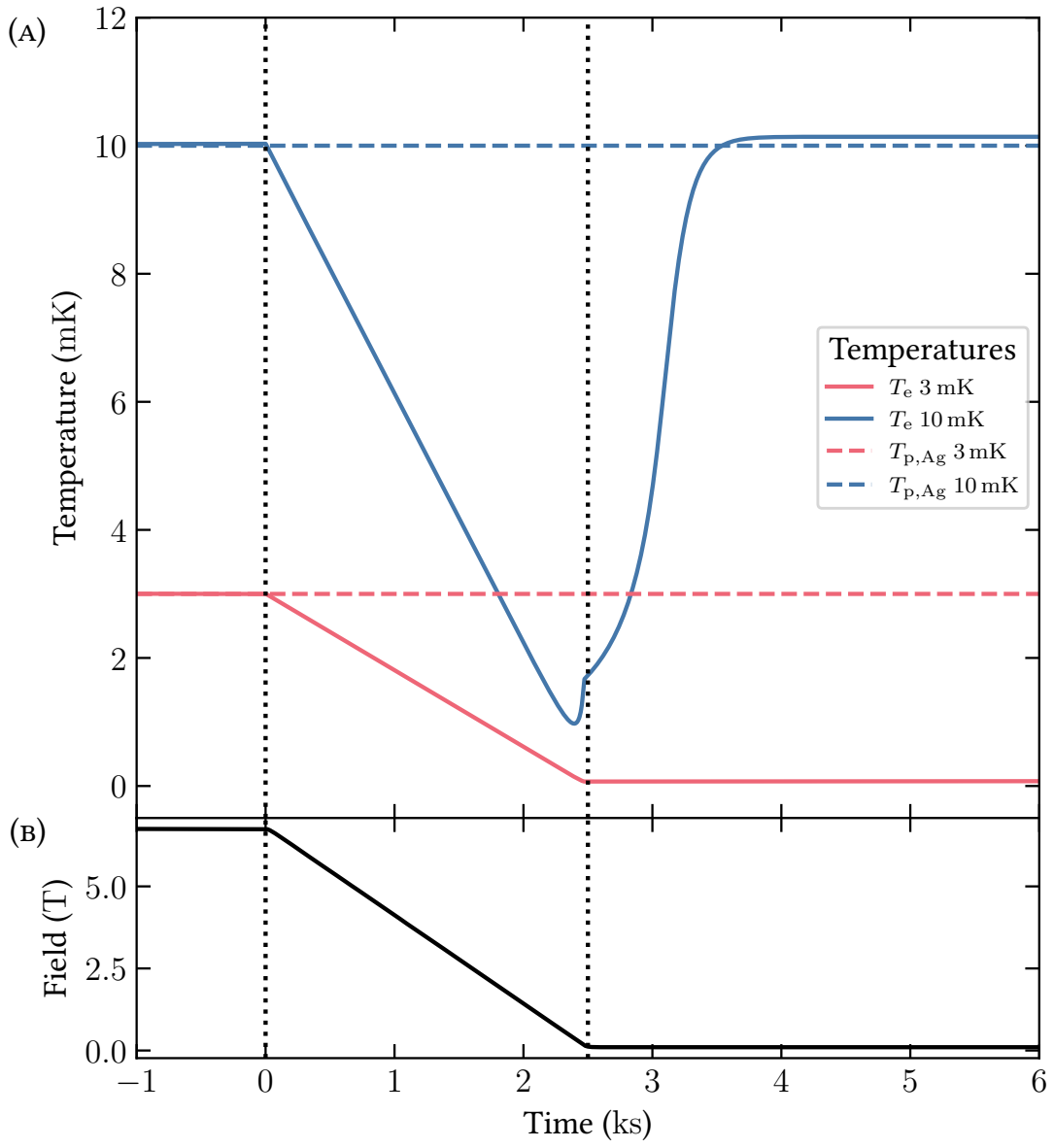

Figure 4.1: Simulated on-chip cooling electron temperatures for two different mixing chamber temperatures. The electron temperatures internal to the cooling island, T_e, are simulated for demagnetisation with 10 (blue) and 3 (salmon) mK mixing chamber temperatures $\left(T_{p,Ag}\right)$. The Kapitza resistance which thermally separates cooling island from mixing chamber is set to $R_{pp} = 1.5 \times 10^{-2}\,\mathrm{K^4 m^2/W}$, the electronic heat leak $\dot{Q}_{leak}$ is 0.1 fW and the magnetic field sweeps from 6.75 T to 100 mT over 2500 s.

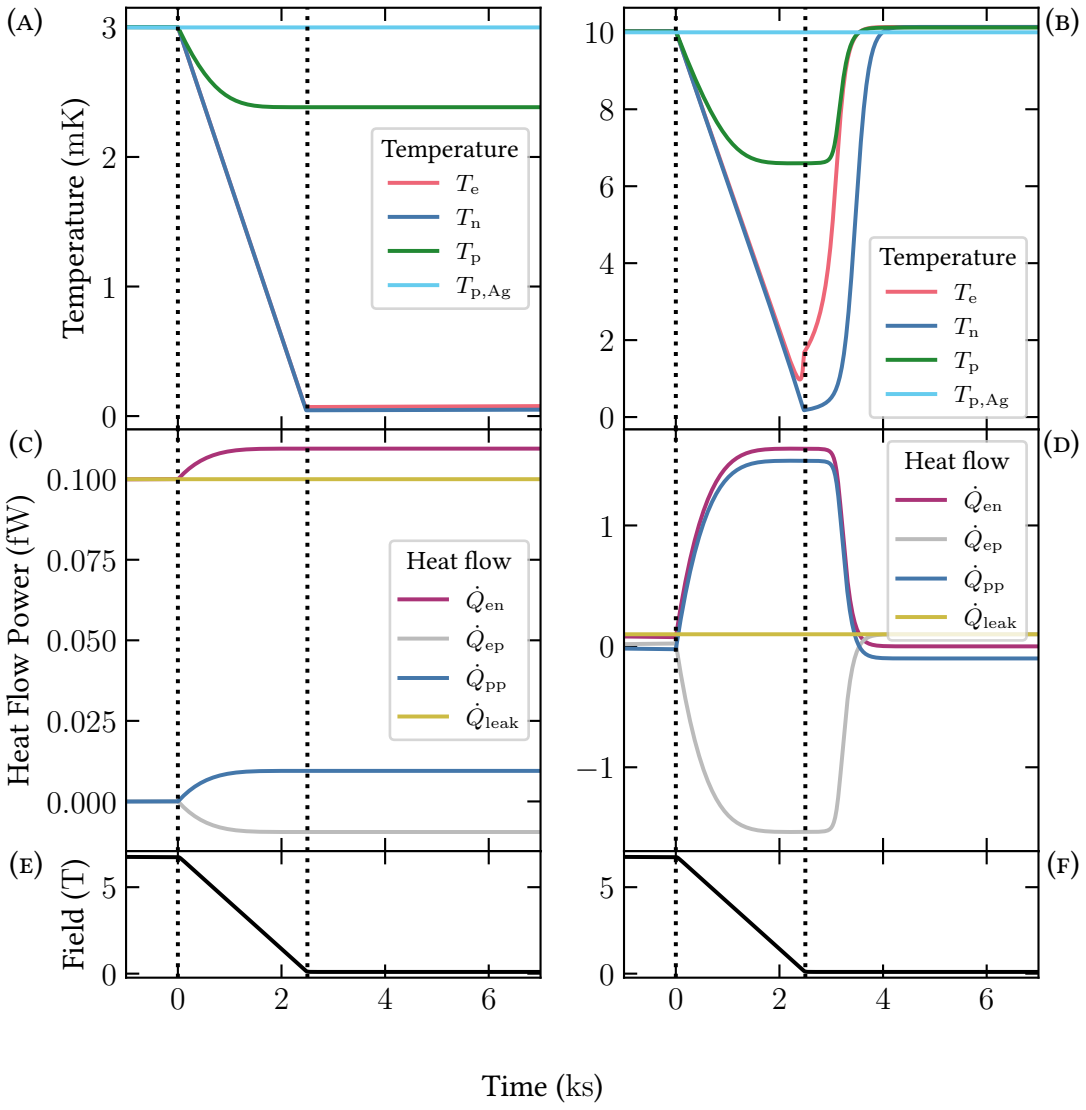

Figure 4.2: Simulated temperatures of thermal baths and heat flows in a copper on-chip cooling island demagnetised in a 3 mK refrigerator, panels (A), (C), and (E). Panels (B), (D) and F show the same systems but simulated in a 10 mK refrigerator.The temperatures internal to a cooling island:T_e, T_n and T_p represent the electron, nuclear spin and phonon baths. The phonon temperature of a silver finger through which the substrate and cooling island are thermalised is shown by $T_{p,Ag}$. (C) & (D) heat flow powers between the above thermal systems, written in the form $\dot{Q}_{xy}$ to represent the heat flow from x to y with pp referring to the phononic boundary heat flow from silver finger to the cooling island. (E) & (F) show the magnetic field strength which sweeps from 6.75 T to 100 mT over 2500 s starting at zero time. Vertical dotted lines are added at zero time and 2.5 ks to mark the start and end of demagnetisation.

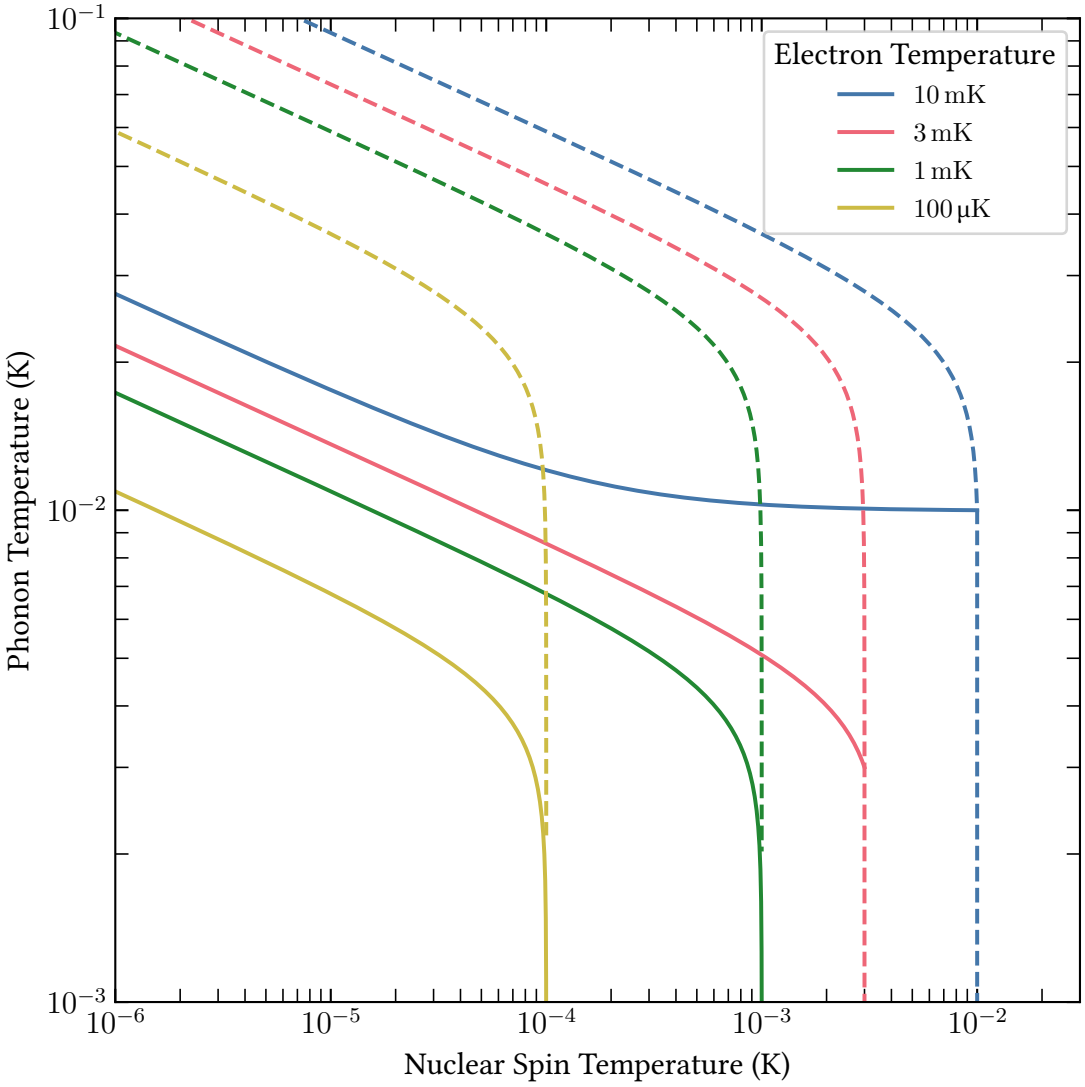

Figure 4.3: For a given electron temperature, points where electron-phonon and electron-nuclear spin heat flows are equal. The lines are calculated using equation (4.4) and are only valid for $T_n < T_e < T_p$. The lines show the equilibrium points in a 100 mT [solid] and a 6.75 T [dashed] magnetic field.

4.3 Effect of Field Strength

Changing the applied magnetic field affects both the electro-nuclear coupling strength [equation (4.1)] and nuclear spin heat capacity

$$C_n = \frac{n\lambda_n \left(B^2 + b^2\right)}{\mu_0 T_{\mathrm{n}}^2} \tag{4.5}$$

[from subsection 2.1.1]. Both are proportional to B^2 when $B \gg b$. At the low-field limit, the effective residual internal field, b, sets a minimum for electron-nuclear heat flow and nuclear spin heat capacity . Final demagnetisation nuclear temperature in the ideal adiabatic case is ultimately controlled by the ratio of final and initial field strengths with

$$T_{\text{final}} = T_{\text{initial}} \left(\frac{B_{\text{final}}}{B_{\text{intial}}} \right) \tag{4.6}$$

[see equation (2.13)]. Maximising this ratio minimises the final nuclear spin temperature. The potential field strength ratio is constrained by the maximum field which can be generated. The minimum magnetic field is physically limited by any residual internal field and also superconducting transitions. Specific to demagnetisation cooling, the electron-nuclear heat flow is proportional to B^2. It is possible that, during demagnetisation, a small enough applied magnetic field may cause electron-nuclear heat flow to reduce such that the electron-nuclear cooling is less than the heat leak and phonon-electron heating, resulting in net warming of the electron bath. With nuclear spin heat capacity also scaling with the square of the field, a low field makes the nuclear spins more susceptible to being overwhelmed by a fixed-power heat leak.

In Figure 4.4, demagnetisation temperatures are simulated with the same magnitude change of field strength but different rates of change. In a 3 mK refrigerator there is no significant difference between the different field sweep rates since heating from

phonons or the heat leak are too weak to overwhelm cooling. In the 10 mK refrigerator case the slower rates have higher minimum electron temperatures. The electrons in this case also start to warm earlier in time before the end of demagnetisation with a lower sweep rate. The electron temperatures and field strengths at the point of electron temperature inflection are shown in Table 4.1. The electrons in the 10 mK

Rate ($mT\,s^{-1}$)	Minimum Field (T)	Electron temperature at minimum (mK)
1.33	0.3208	1.111
2.66	0.2991	0.9740
5.32	0.2886	0.9162

Table 4.1: Electron temperatures and applied field strengths in a 10 mK refrigerator for the points of electron temperature inflection in Figure 4.4.

refrigerator generally start to warm around 300 mT. This is not solely a product of field since changing the refrigerator temperature or heat leak [see Figure 4.7] affects when this warming occurs. The 300 mT limit observed is then a specific combination of field, electron-phonon heating and the heat leak acting over the full duration of demagnetisation. Demagnetising over a longer time ensures that the systems internal to the copper cool down slower and take longer to decouple from the refrigerator. This increases the time over which heat-flow from the refrigerator can erode nuclear cooling capacity.

It should be noted that this simulation and thermal model of demagnetisation does not take into account eddy current heating which is induced in a metal by a changing magnetic field. Eddy heating is described by

$$\dot{Q}_{\text{eddy}} = \frac{\sigma A V}{8\pi}\left(\frac{\partial B}{\partial t}\right)^2 \tag{4.7}$$

for a cylinder under an applied magnetic field B which is parallel to the cylinder's length axis with electrical conductivity σ and volume V. The cross-sectional area of the cylinder A, is defined as a continuous plane through the metal, perpendicular to B.

The dimensions of the copper block used in this simulation are 205 µm × 39 µm × 6.5 µm with the device oriented such that the cross-sectional area perpendicular to the field is 39 µm×6.5 µm. Residual resistivity [and thus electrical conductivity] of copper can vary greatly [6]. Estimated eddy current heating for a copper block of this size varies from 10^{-23} W to 10^{-20} W depending on this resistivity. With electro-nuclear heat flow during demagnetisation on the order of 10^{-18} W [see section 4.2], eddy heating contributions are negligible for this device.

Increasing the field strength swept over in demagnetisation results in lower nuclear spin temperatures after demagnetisation. Equation (2.13) implies that doubling the maximum field strength halves the final nuclear temperature in the ideal adiabatic case. In these simulations that would require increasing the initial field from 6.75 to 13.5 T and keeping the same final field of 100 mT.

Simulated demagnetisation temperatures with this modified field profile are shown in Figure 4.6. For both refrigerator temperatures, the increased magnetic field strength sweep lowers the final electron temperature by roughly a factor of two. Warming at the low-temperature limit is dominated by the fixed-power heat leak. A reduced final temperature then results in refrigerator and island taking longer to return to equilibrium temperatures. In the 10 mK refrigerator the electron temperature experiences the same warming before demagnetisation ends for both field profiles. The subsequent warming takes twice as long to reach refrigerator temperature. Increasing the total magnetic field sweep does reduce nuclear spin and device electron temperatures but is not the solution to the rapid warming in a 10 mK refrigerator. Further increases of ΔB are also not feasible, with maximum field strengths in sweepable superconducting magnets rarely beyond 14 T.

With a sufficiently powerful magnet, demagnetisation can start and end with a stronger field strength but preserve the same temperature reduction by keeping the

field ratio in equation (2.13) constant. Under this ratio condition there should be no change in electron-phonon coupling but electron-nuclear heat flow and nuclear heat capacity will increase by B^2, making the electron-nuclear system less susceptible to fixed-power heat leaks.

In Figure 4.5 two simulated demagnetisations field profiles are shown. The first profile has a field which sweeps from 6.75 T to 0.100 T. The second maintains the same B_{final} / B_{initial} ration but with higher strengths, sweeping from 13.5 T to 0.200 T. Both field profiles, in the ideal case, will result in a final nuclear spin temperature of 0.0148 T_{initial} by equation (2.13). For both of the fridge temperatures, demagnetising from a higher field strength does not significantly effect the cooling power of demagnetisation. In a 3 mK refrigerator, the stronger final field moves the equilibrium electron temperature closer to the nuclear temperature, such that they are indistinguishable in Figure 4.5 panel B. This results from the doubling of the final field which quadruples the electron-nuclear heat flow for the same temperatures.

Another feature of the stronger field strength is slower warming after demagnetisation. This slower warming is seen in electron, nuclear and phonon temperatures internal to the island. With no significant change in base temperature between the two field ramps, and thus no significant change in heat flow, this slower warming is a result of the field-dependent heat capacity of the nuclear spins. By equation (4.5), the heat capacity of nuclear spins increases with the square of the magnetic field. In this case that creates four times the heat capacity at the lowest temperature for the the higher field demagnetisation. An increased heat capacity results in a nuclear spin temperature which is less susceptible to heating. A higher starting and final field is thus desirable for on-chip demagnetisation which stays cold for longer.

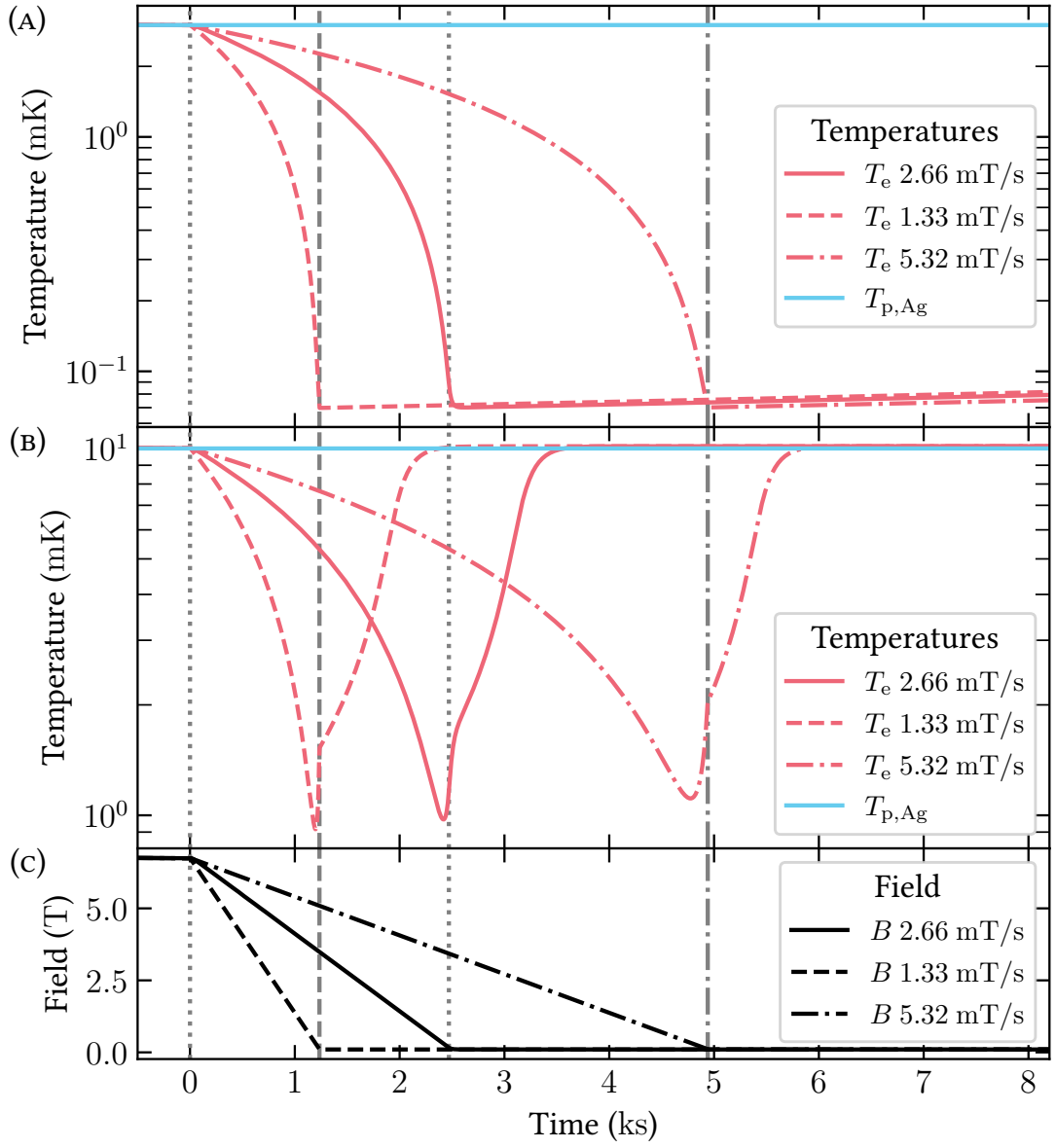

Figure 4.4: Simulated temperatures in 10, (A), and 3, (B), millikelvin refrigerators demagnetised with the same field but at different rates. Panels (A) & (B) show electron temperatures when demagnetised at 1.33 [dashed] 2.66 [solid] and 5.32 [dot-dashed] mT s^{-1}. All demagnetisations start at zero time, sweeping from 6.75 to 0.1 T. Vertical grey lines mark the start and end of the three demagnetisation sweeps. The field profiles are shown in panel (C).

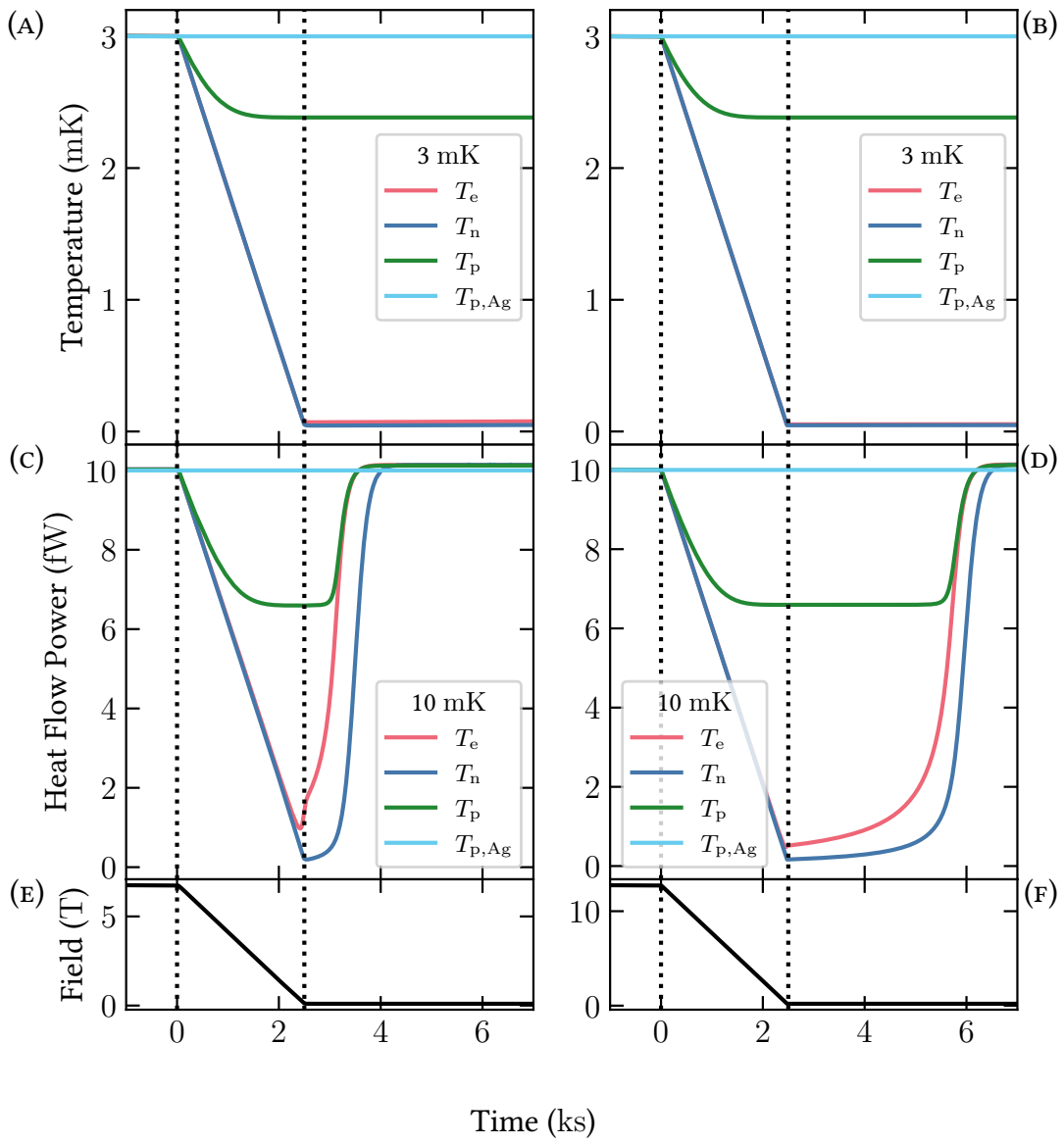

Figure 4.5: Simulated temperatures in 10 and 3 mK refrigerators demagnetised with the same B_{final} / B_{initial} but different starting field strength. Panels (A) & (C) show the thermal systems under demagnetisation in 10 and 3 mK refrigerators respectively, with a field sweeping from 6.75 T to 100 mT over 2500 s. Panels (B) & (D) show the same fridge temperatures demagnetised with the same $B_{\text{final}}/B_{\text{initial}}$ change in field strength but sweeping from 13.5 T to 200 mT. The field sweeps are shown in (E) & (F) with vertical dotted lines drawn across all panels to mark the start and end of demagnetisation.

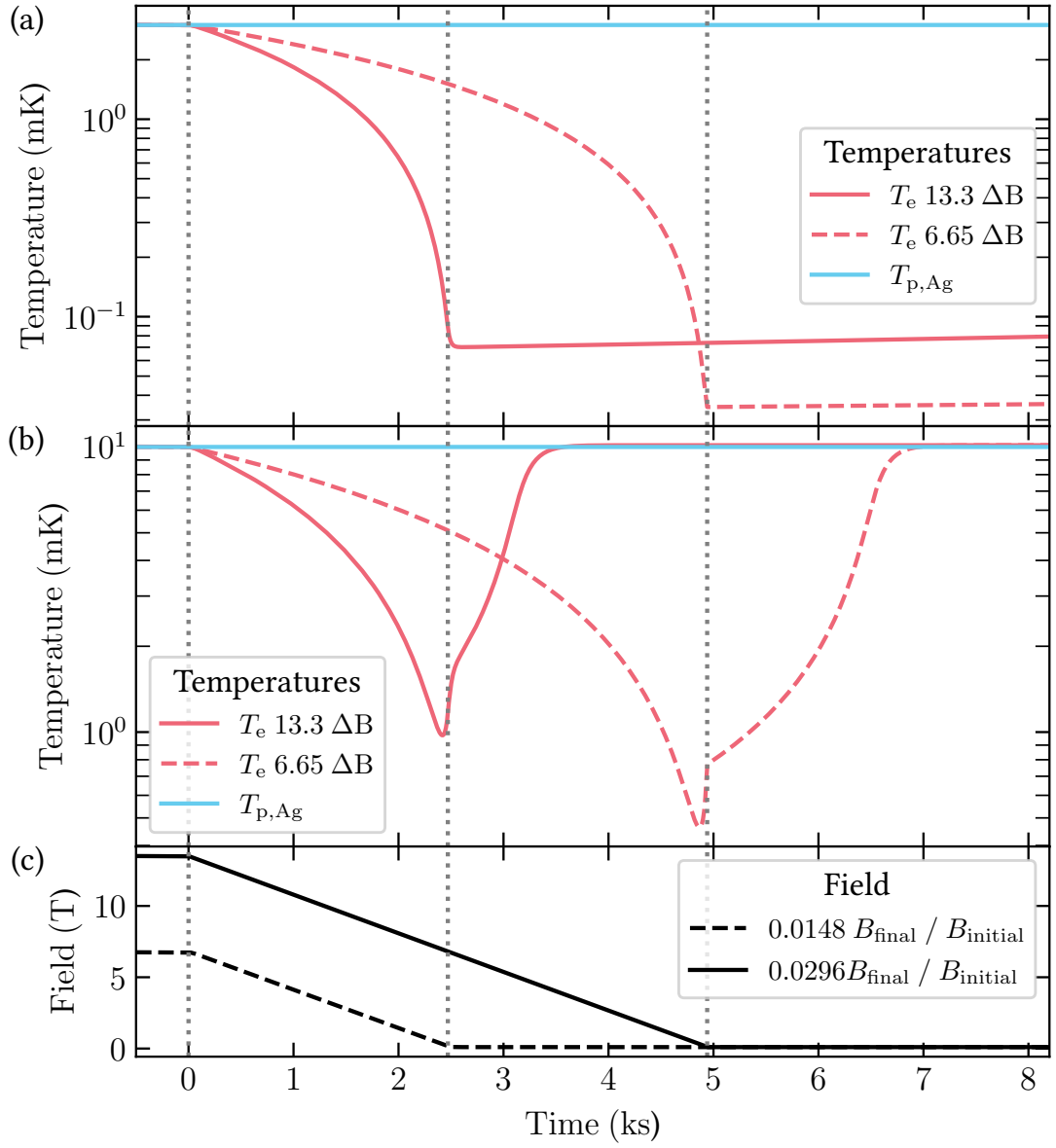

Figure 4.6: Simulated temperatures in 10, (A), and 3, (B), millikelvin refrigerators demagnetised with the changing difference in magnetic field strength at constant rate. Panels (A) & (B) show electron temperatures during and after demagnetisation for 3 and 10 mK fridge temperatures respectively. All demagnetisation starts at zero time, sweeping from 6.75 and 13.4 to 0.1 T. Vertical grey lines mark the start and end of the demagnetisation sweeps. The field profiles are shown in panel (C).

4.4 Effect of Heat Leak

The 0.1 fW heat leak used in these simulations up to this point is based on the experimental heat leak measured with a coulomb blockade thermometer in a Lancaster dilution refrigerator [1]. This single heat leak represents a summation of numerous undesirable heat-flows from numerous sources into the experiment. Electrical noise, magnetic noise, thermal radiation and Weidemann-Franz conduction down measurement lines are particular examples of heat-leak sources. In this simulation the heat leak can be varied and its influence on on-chip demagnetisation studied. This is a purely theoretical exercise as this heat leak is always minimised in low temperature experiments and is not a parameter which can be freely tuned to a specific power.

Figure 4.7 shows simulated demagnetisations in a 10 mK refrigerator for a range of heat leak powers from 0.01 fW to 350 fW. The span of heat leaks is plotted on three separate subfigures for convenience but these three spans also help illustrate the different regimes created by the heat leaks: heat leaks controlling temperature, mixed regime and heat leaks controlling hold time. Before demagnetisation and for 22 fW to 350 fW heating, the island electrons do not pre-cool to the refrigerator base temperature. The heat leak, as per the thermal model, directly heats the electrons. With electrons then hotter than the refrigerator, the on-chip island is cooled via the electron-phonon and refrigerator to island phonon links. These links vary with temperature [see section 4.2], reaching an equilibrium point when electron-phonon heat flow matches the heat leak into the electrons.

With a 350 fW heat leak the equilibrium temperature for electrons is roughly 30 mK above the fridge temperature and demagnetisation cooling is almost completely overwhelmed. Elevated starting temperatures for demagnetisation harm cooling performance, with electron-phonon coupling increasing with the square of temperature and electron-nuclear spin cooling constant with higher temperature [discussed in

section 4.2]. With smaller heat leaks, the equilibrium electron temperature approaches the mixing chamber temperature and the demagnetisation performance is improved. Decreasing the heat leak results in lower minimum electron temperatures and electrons cooling for a longer time during demagnetisation.

Figure 4.8 shows the same heat leak powers but in a 3 mK refrigerator. This lower base shows the same significant pre-cooling offsets in electron temperature as the hotter refrigerator for heat leak powers above 20 fW. Between 0.157 and 12.86 fW the electrons temperatures go from warming during demagnetisation to cooling for the full time and staying cold afterwards. At the lowest heat leak powers, 0.01 fW to 0.0905 fW, the electrons are not offset above fridge temperature and instead the heat leak power controls the minimum electron temperature and hold time below 1 mK.

It is clear that with a 10 mK dilution refrigerator, the experimental heat leak into the electron bath is not the limiting parameter for enabling on-chip demagnetisation cooling, the fridge temperature itself is more important here. With a 3 mK refrigerator, controlling the heat leak becomes more more important. Even a small change in heat flow, reducing the heat leak from 1 fW to 0.01 fW, takes on-chip cooling from failing to reach and stay at submillikelvin electron temperatures to cooling to below 50 µK and remaining below 100 µK for well over 17 ks. The strong changes in hold times and temperatures are highlighted in Figure 4.9. This figure shows heat leak powers below 3 fW for the full simulated duration of 17 ks. The changes in hold time and temperatures demonstrate how a small change in heat leak can greatly influence on-chip demagnetisation performance.

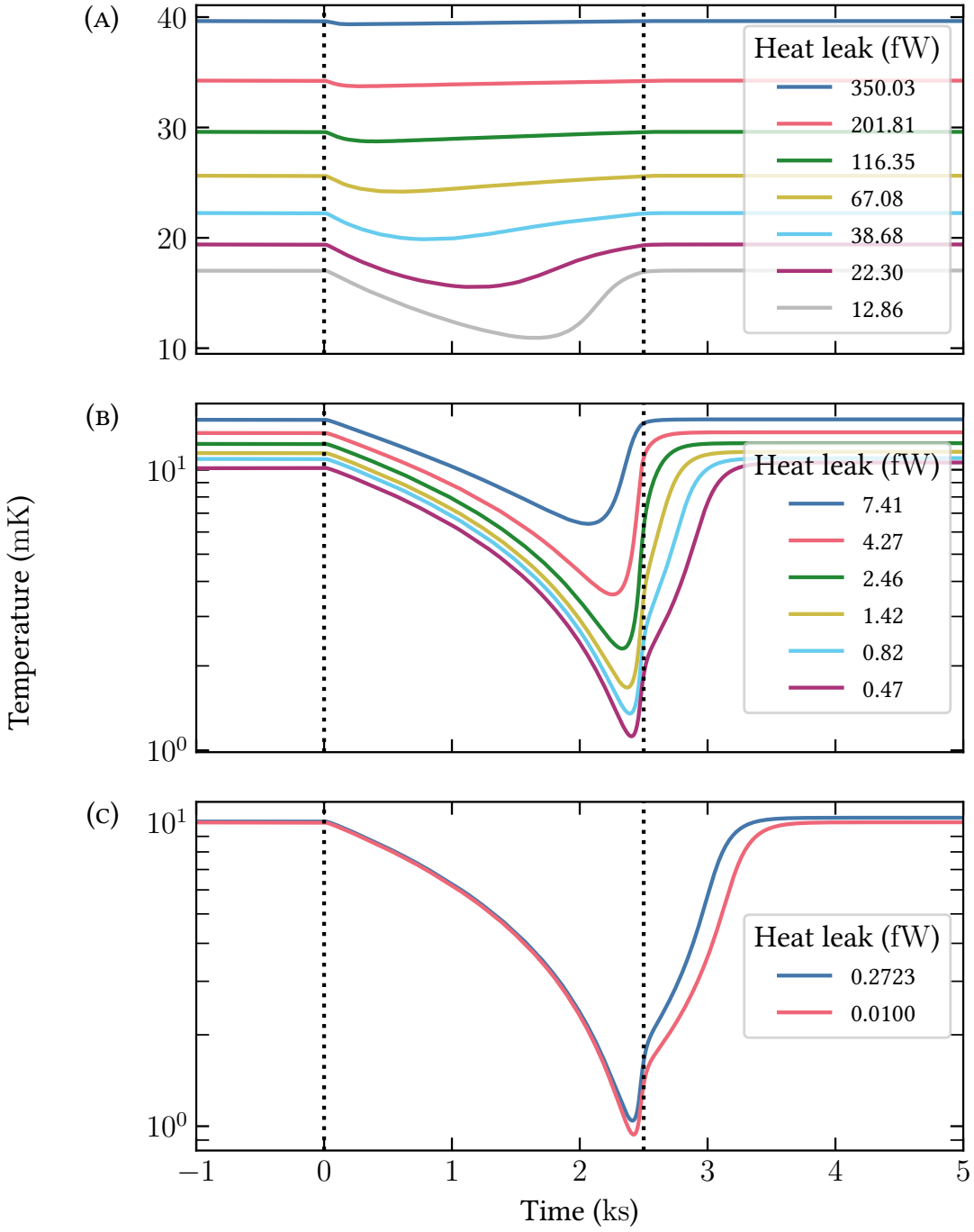

Figure 4.7: Simulated temperatures under demagnetisation in a 10 mK refrigerator with changing electronic heat leak. Heat leaks are spaced from 350 fW to 0.01 fW. The three different subgraphs show two different behaviours of electron temperature: heat-leak dominated (A) and mixed behaviour (B), (C).

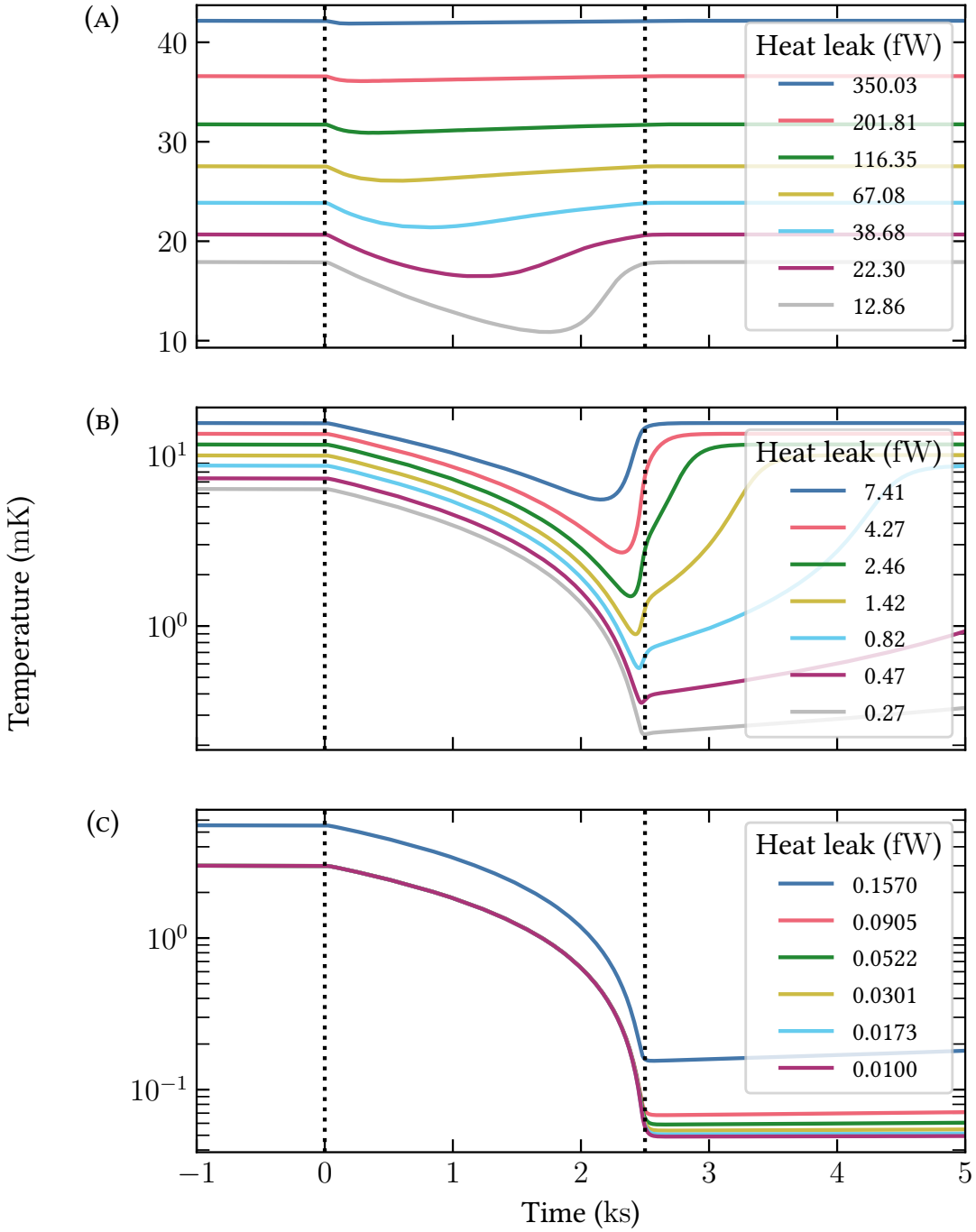

Figure 4.8: Simulated temperatures under demagnetisation in a 3 mK refrigerator with changing electronic heat leak. Heat leaks are spaced from 350 fW to 0.01 fW. The three different subgraphs show three different behaviours of electron temperature: heat-leak dominated (A), mixed behaviour (B) and heat leaks controlling hold time (C).

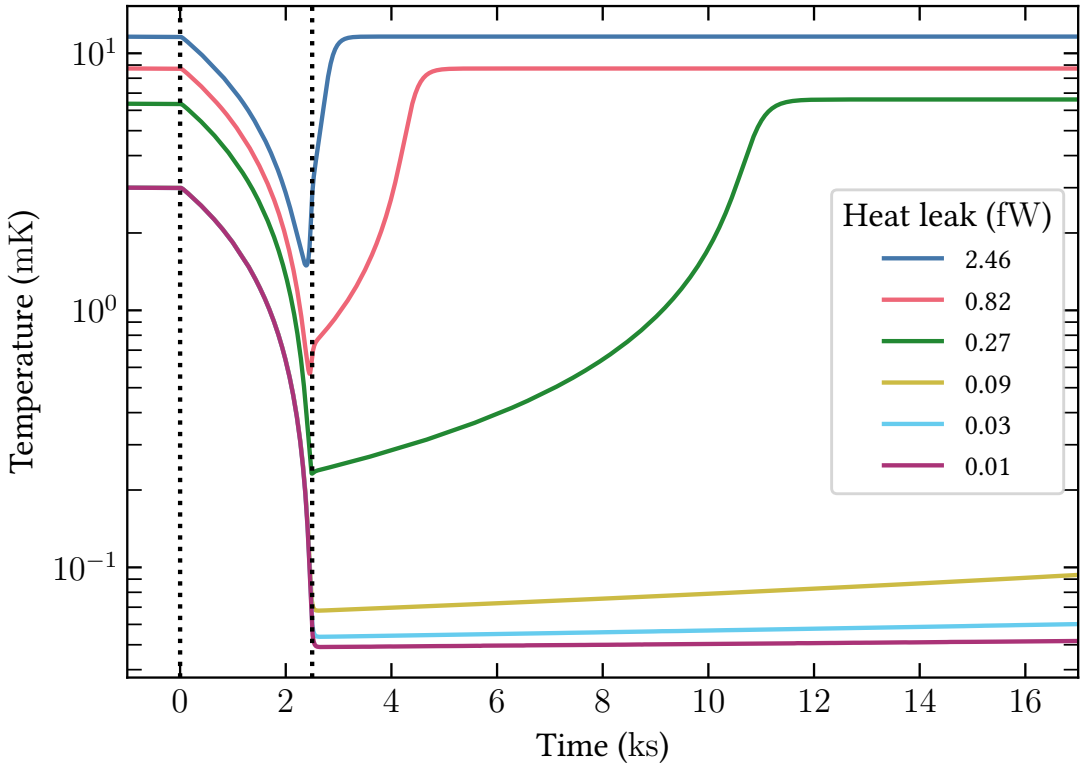

Figure 4.9: Simulated temperatures under demagnetisation in a 3 mK refrigerator with changing electronic heat leak. A selection of heat leaks spanning 2.46 fW to 0.01 fW are taken from Figure 4.8 and shown for the full simulated 17 ks after demagnetisation begins.

4.5 Changing the thermal link between fridge and device

During demagnetisation and subsequent warm-up, energy flows into the on-chip electrons from the refrigerator. The heat-flow from the refrigerator to the on-chip coolant is controlled by a total Kapitza resistance, R_{pp}, which moderates phonon transport through stacked layers of materials between the copper island and silver thermalisation layer. The heat flow from silver thermalisation layer to on-chip copper can be written as

$$\dot{Q}_{\mathrm{pp}} = \left(T_{\mathrm{p,Ag}} - T_{\mathrm{p}}\right)/R_{\mathrm{pp}} \tag{4.8}$$

$$= \left(T_{\mathrm{p,Ag}} + T_{\mathrm{p}}\right)^{2} \left(T_{\mathrm{p,Ag}}^{2} - T_{\mathrm{p}}^{2}\right) A/\left(8\, r_{\mathrm{pp}}\right) \tag{4.9}$$

as discussed in section 2.1. This resistance to thermal phonon transport, R_{pp}, effectively limits the heat flow between refrigerator and device.

Prior to demagnetisation, the coldest point in this on-chip cooling thermal model [Figure 2.2] is the silver thermalisation layer. Under this condition, heat predominantly flows into the electrons from the heat leak, $\dot{Q}_{\mathrm{leak}}$, and the electrons lose heat to the phonons at a rate dictated by $\dot{Q}_{\mathrm{pe}}$ [see equation (4.2)]. For a constant $\dot{Q}_{\mathrm{pe}}$, the heat flow from electrons to internal phonons must be matched by a flow of heat from the internal phonons to the phonons in the silver thermalisation layer $\dot{Q}_{\mathrm{pp}}$. This balance is the cause behind electron temperatures being offset above the refrigerator base temperature prior to demagnetisation, as discussed in the previous section. By equation (4.8), as $\dot{Q}_{\mathrm{pp}} \propto R_{\mathrm{pp}}^{-1}$, for two otherwise identical samples with the same internal temperatures, the sample with a lower R_{pp} will have a larger $\dot{Q}_{\mathrm{pp}}$ and as such will cool down quicker. A lower R_{pp} reduces the offset temperature in the same manner since the required $\dot{Q}_{\mathrm{pp}}$ to equal the heat leak is produced by a smaller temperature difference. The desirable

benefits of shorter pre-cooling times and a lower temperature offset are juxtaposed by increased fridge-device heat flow during demagnetisation and subsequent warm up. This erodes the cooling power of the nuclear spins, resulting in higher minimum electron temperatures and shorter hold times. This trade off can be summarised in Table 4.2.

	Higher R_{pp}	Lower R_{pp}
Cooling performance	Improved	Diminished
Pre-cooling time	Increased	Reduced
Initial offset temperature	Increased	Reduced

Table 4.2: The effects of varying R_{pp} on an on-chip cooling island.

Figure 4.10 shows three simulated devices with three different R_{pp} values at two different fridge temperatures. Figure Figure 4.10 panel A shows that in a 3 mK fridge, changing R_{pp} has no significant effect on demagnetisation performance as heat flow from the refrigerator is already sufficiently limited by temperature. A weaker R_{pp} limits the minimum electron temperature achieved. In the 10 mK case, Figure 4.10 panel B, the difference is much more pronounced. With a lower R_{pp}, electrons start to warm earlier in the demagnetisation and the rate of cooling prior to this is reduced. This comes as a result of the stronger fridge-device thermal connection overwhelming the nuclear cooling. The increased R_{pp} of $1.0\,\mathrm{K^4m^2/W}$[dot-dashed line] sufficiently limits the heat flow from the fridge to the point where the electrons continue to cool for the full duration of demagnetisation and stay cold for some time afterwards. Of the parameters investigated so far, this is the parameter that has the largest impact on the performance of on chip cooling in a 10 mK fridge, with a potential to run experiments at millikelvin temperatures.

In the previous section, we discussed how sensitive demagnetisation is to heat leaks, especially in the critical range of 0.01 fW to 1 fW. Figure 4.11 demonstrates the sensitivity of a device and how much more pronounced these effects are with an

increased R_{pp}. A large heat leak, as discussed in the previous section, creates a large initial offset, harming the potential minimum electron temperature. It also reduces the hold time. While R_{pp} doesn't have any effect on the hold time, it does increase the temperature offset given the same heat leak, as discussed above. This is evidenced by the simulated electron temperatures with a 0.09 fW heat leak, shown in Figure 4.11 panel C. With an increased R_{pp}, this simulation has a notable temperature offset prior to demagnetisation compared to the same heat leak power simulated in Figure 4.7 panel C. With this increased thermal resistance, demagnetisation to microkelvin electron temperatures in a 10 mK refrigerator becomes possible but controlling experimental heat leaks is now critical to this success.

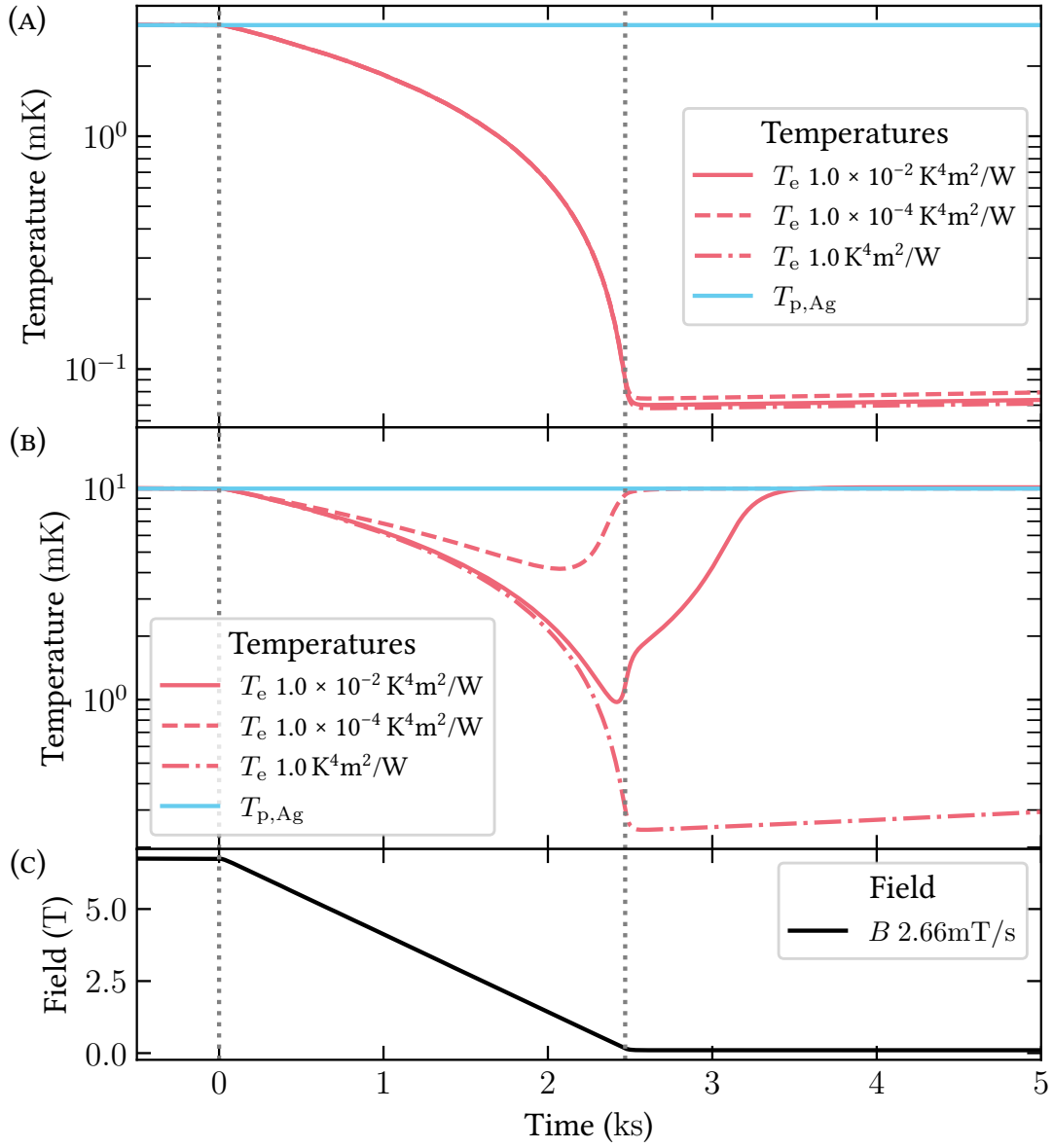

Figure 4.10: Simulated temperatures under demagnetisation, modifying the interfacial Kapitza resistance between thermometer and refrigerator. Subfigures (A) & (B) show the effect of changing interfacial resistance in 3 and 10 mK refrigerators. (C) shows the field profile for demagnetisation with the dotted grey lines marking the beginning and end of the field sweep.

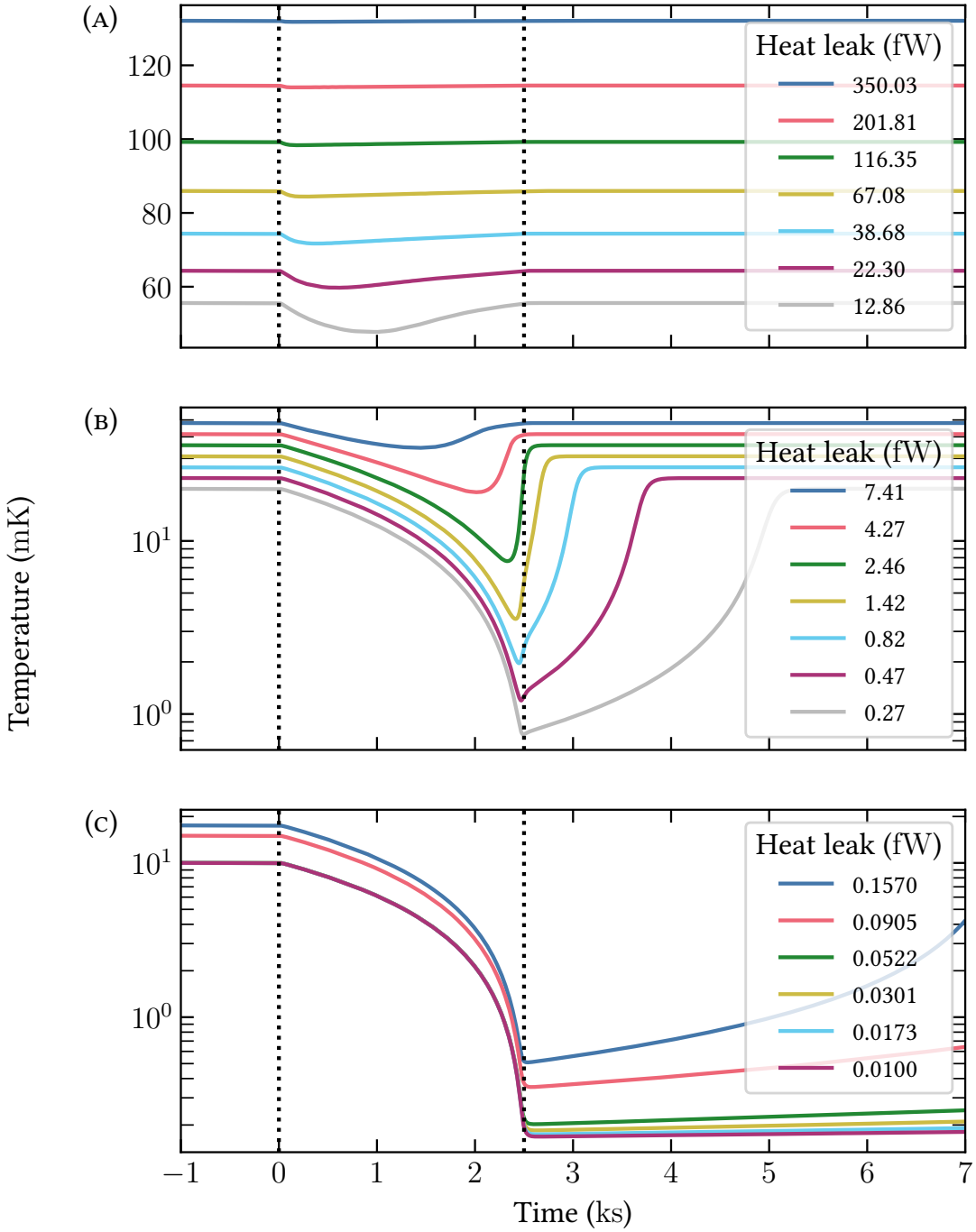

Figure 4.11: Simulated demagnetisation of a demagnetisation island in a 10 mK refrigerator with increased interfacial thermal resistance, showing the importance of heat leak with this modified resistance. The three subfigures show three different spans of heat leaks, separated for clarity.

4.6 Other metals

Simulations of demagnetisation in this chapter have used a copper refrigerant to be consistent with CBT experiments performed in Lancaster. The demagnetisation performance of a metal depends on numerous properties specific to each metal and can vary greatly. The properties relevant to this simulation are shown in Table 2.1 for a number of different metals. The effects of these properties on demagnetisation cooling are discussed in subsection 2.1.5.

While the simulation can be run with these properties to compare refrigerants, there are some material differences which are difficult to account for. The Kapitza resistance is specific to the boundary dimensions, roughness and materials used [47]. Theoretical calculations of boundary resistance are possible and often in agreement with experimental data for bulk materials [74–76]. The multiple stacked layers of thin-film materials used in this work may make such calculation difficult so it is assumed that all refrigerants will have a constant Kapitza resistance, equal to the resistance measured with copper in this work. Explorations of changing nuclear refrigerant are further limited by a lack of experimental measurements of electron-phonon coupling constant for the metals in Table 2.1.

Figure 4.12 shows demagnetisation in a 10 mK refrigerator with three different refrigerants. The refrigerants used are copper, indium and aluminium. Electrons in copper cool down to ~1 mK, start to warm before demagnetisation ends continue warming to 10 mK in under 1 ks. Using aluminium refrigerant, the minimum electron temperature is reduced to <600 μK, begins to warm before demagnetisation ends and returns to 10 mK in 4.5 ks. The best-performing refrigerant is indium, which cools electrons to below 200 μK and has a hold time below 300 mK of over 11 ks.

By equation (2.19), increasing the Curie constant and reducing Korringa constant will both increase electron-nuclear heat flow and cooling power. In on-chip demagneti-

sation, this increase will keep electron temperatures closer to nuclear spin temperatures. The electron-phonon heat flow required to overwhelm cooling will also be increased, lowering minimum electron temperatures. A raised Curie constant will also increase the nuclear heat capacity, making nuclear spins less susceptible to heat leaks. This is reflected in the simulated temperatures by the lower minimum electron temperatures and slower warming after demagnetisation of indium and aluminium.

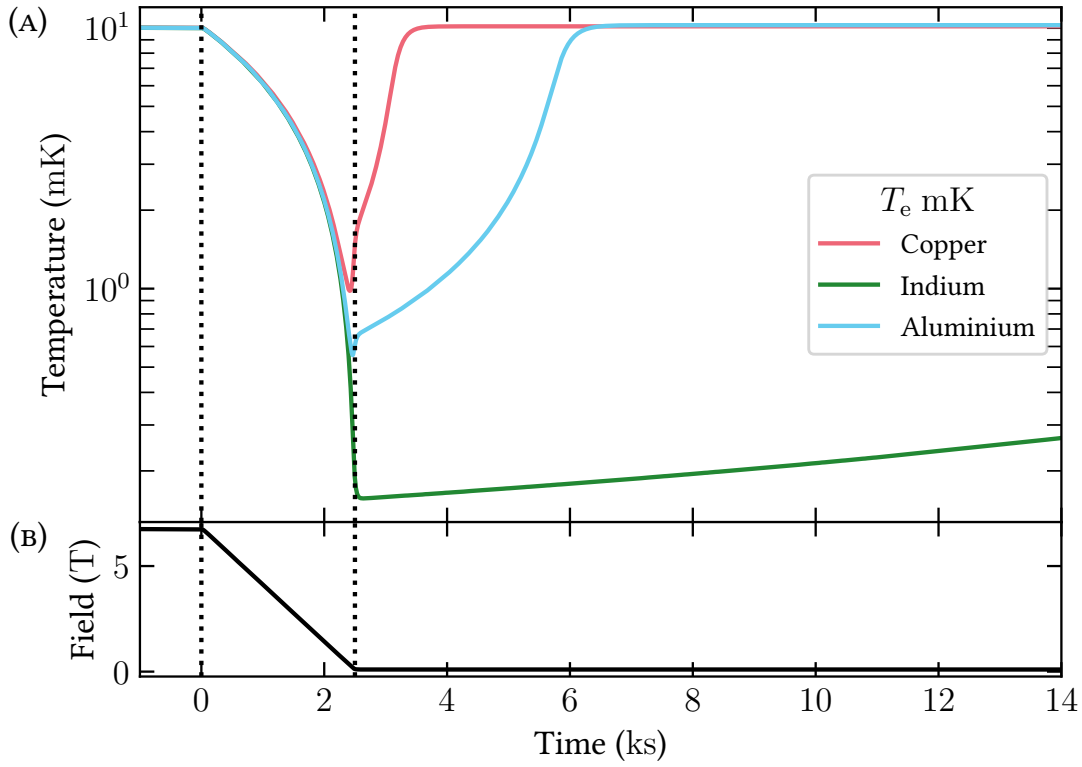

Figure 4.12: Simulated electron temperatures in an on-chip island demagnetised in a 10 mK with three different refrigerants. Copper (salmon), indium (green) and aluminium (cyan) islands with the same number of moles are demagnetised in otherwise identical refrigerators. The heat leak is fixed at 0.1 fW and all metals are assumed to have $R_{pp} = 1.0\,K^4m^2/W$.

Chapter 5

On-chip cooling of a niobium nitride thermometer

This chapter describes progress towards cooling a niobium nitride thin-film resistor with indium on-chip refrigerant. The chapter focuses on the electroplating of indium refrigerant and discuss how a similar plating technique can be used to make superconducting shells.

5.1 Testing on-chip cooling

The goal of this project is to apply on-chip demagnetisation cooling, as developed in Lancaster coulomb blockade thermometer (CBT) experiments, to cooling electrons to microkelvin temperatures in other devices. This is motivated by the complexities of using and understanding CBT dynamics which make evaluating the performance of on-chip cooling difficult. CBTs are also uniquely well-suited to on-chip cooling as islands of refrigerant can be placed between tunnel junctions, inside the CBT, without greatly impacting the thermometer's performance. To develop on-chip demagnetisation as a technique for broader nanoelectronic cooling, there is a need to test and demonstrate

its capability with other thermometers and devices.

Electronic thermometers which are sensitive at millikelvin temperatures can broadly be placed into two classes. Junction-based thermometers, such as CBTs quantum dots and superconductor-metal junctions, rely on restricting the conduction of electrons across a potential gap or barrier [14]. In this they are sensitive to electron temperature as a function of population of electrons with sufficient energy to cross the junction. Noise thermometers for comparison measure the current or magnetic noise created by the random movement and fluctuation of conduction electrons in metals [77–79]. They measure electron temperature as a function of the Johnson-Nyquist noise [80, 81] produced by thermal electrons.

An ideal thermometer for testing on-chip cooling should be primary, such that it does not need to be calibrated to a second thermal system or thermometer with a short measurement time to measure rapidly-changing temperatures. It also need to be sensitive to electron-temperature in the millikelvin regime. Since this study has used demagnetisation cooling, the thermometer should preferably not have a magnetic field dependence.

A resistive thin-film thermometer made from niobium nitride was chosen as a suitable thermometer candidate. At low temperatures the conduction electrons in an impure metal can become weakly localised, conductance is then dominated by electrons tunnelling between potential wells. This temperature-dependent conductance can be described by the Anderson [82, 83] or Efros-Shkolvskii [84] models. Thin films of niobium nitride have been found to have a temperature-dependent conductance from 77 K down to millikelvin temperatures with evidence suggesting a hopping conductance at the lowest temperatures [85]. This is a secondary thermometer and will need to be calibrated against known reference points, but the electron-sensitivity near saturation and the simple nature of resistive four-terminal measurements make it a suitable

thermometer for this study.

This work plans to make a four-terminal resistance measurement of a thin-film niobium nitride thermometer. Along the four terminal leads, islands of demagnetisable material can be placed to create volumes of cold electrons. These islands will be in electrical contact with the measurement circuit on both sides of the thermometer on-chip. The expectation is that these islands will cool electrons in the measurement circuit and thermometer, resulting in a measured drop of conductance. The refrigerant of choice for this study is indium owing its higher cooling power than copper [26], as discussed in subsection 2.1.5 and section 4.6. The measurement leads have large pads made from gold deposited on a titanium layer, itself deposited on a standard silicon wafer. It is on these pads that the refrigerant will be grown.

5.2 Indium electroplating for on-chip islands

While metals other than copper show great potential for OCDC (see subsection 2.1.5), electrodeposition of them is not well-researched. There are commercial solutions for indium electroplating [86] which are primarily designed for plating of bump-bond circuit interconnects, gasket seals and aeronautics bearings. Developing a chemical mix tailored to nanofabrication is no simple and straightforward endeavour but there is still potential to use these commercial mixes, adjusting current density and the electrochemical voltammetry cycle to optimise deposited coatings of metal. Electroplating chosen as a deposition method due to the lower inbuilt strain of large electroplated structures and the lower cost of deposition when compared to other deposition methods [55].

The plating in this study is performed using a commercial sulfamic acid electroplating mix. The chemical composition of this mix is listed in Table 5.1.

Electrodeposition in this work is built upon the plating methodology of Yurttagül

Name	Formula	Quantity ($g\,L^{-1}$)
Indium Sulfamate	$H_6InN_3O_9S_3$	105.36
Sodium Sulfamate	H_2NNaO_3S	150
Sulfamic Acid	HSO_3NH_2	26.4
Sodium Chloride	NaCl	45.84
Dextrose	$C_6H_{12}O_6$	8.0
Trielthanolamine	$(CH_2OHCH_2)_3N$	2.29

Table 5.1: Chemical composition and concentration of an indium electroplating bath. Reproduced from Slattery [86].

[44] and Yingtao [87] with modifications to simplify the fabrication processes. An asymmetric pulse-reverse plating cycle, where each positive current pulse is followed by a negative pulse of a shorter duration, is suggested to encourage large crystal growth and result in more even growth than forward cycle only [87].

Prior to plating, the device is covered in AZ-40XT photoresist and small windows opened for the indium growth. This resist was chosen as it is thick-stacking, enabling sharp walls of up to 100 µm tall and it is highly resistant to acids. The purpose of the photoresist is to protect the thermometer circuitry from being damamged by the acidic electroplating bath during electroplating. In initial platings, it was found that any titanium accessible to the acid would be oxidised and readily removed during the reverse portion of the plating cycle. This caused electrical lines and the growth pads to fall off the silicon substrate.

The plating is performed using an asymmetric pulse-reverse cycle of $20\,mA\,cm^{-2}$ for 1.5 ms, $-10\,mA\,cm^{-2}$ for 0.5 ms then 8 ms of zero current. This cycle was repeated until desired deposit thickness was achieved. Prior to the cycle there is a 500 ms pulse to seed the gold with indium and protect it from etching during the reverse portion of the cycle. A 10% solution of sulphuric acid was used to clean and activate the growth pads prior to plating. A representation of indium electrodeposition growth is shown in figure 5.1.

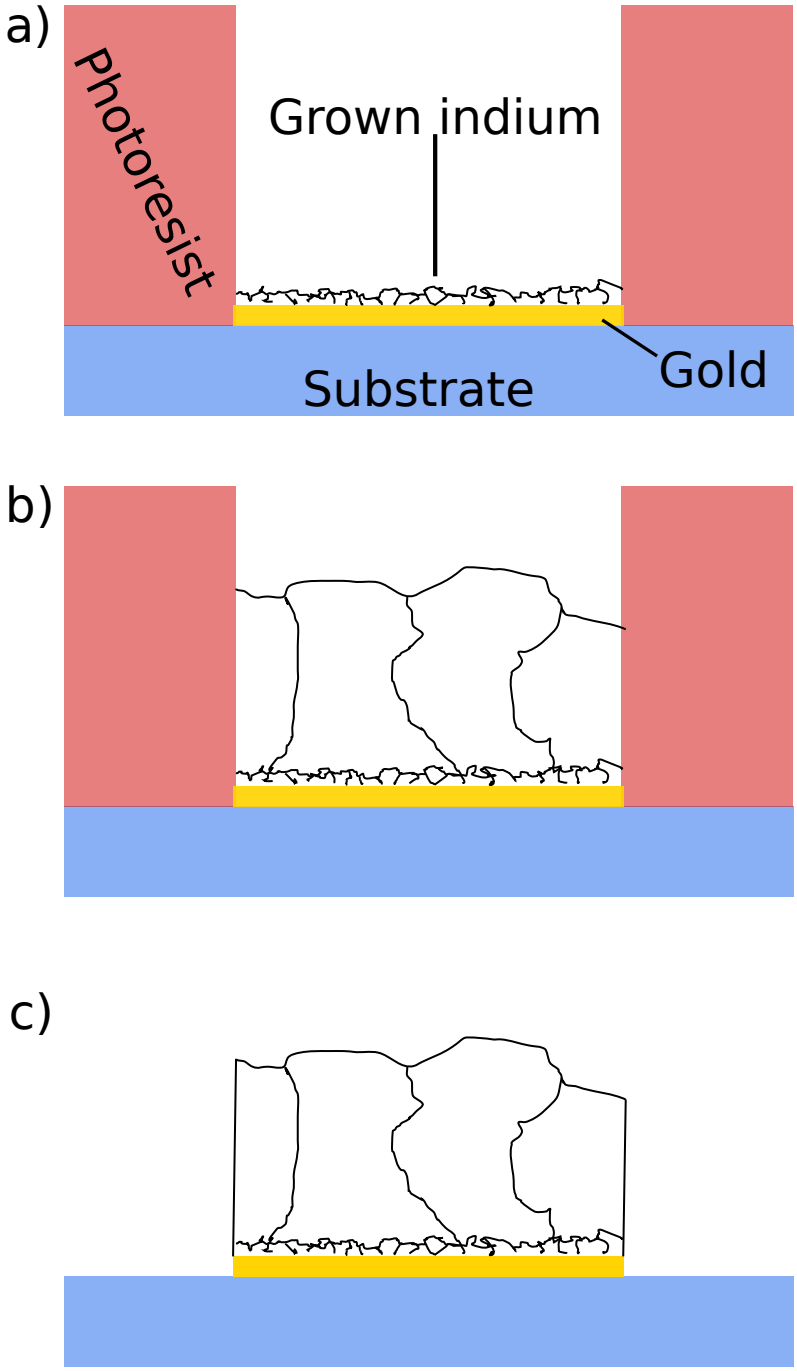

Figure 5.1: Steps of indium growth. a) DC seeding of a thin layer of indium to cover the gold. b) asymmetric alternating current encourages growth of large crystal domains. c) photoresist is removed leaving behind the indium structure.

5.3 Electroplated indium examples

Two test chips were coated in indium using the duty cycle described at the end of section 5.2. The first was grown for 7200 seconds and electron microscopy images of the indium layers are shown in figures 5.2 and 5.3. Figure 5.2 shows a number of different regions with different and inconsistent growth behaviours. Panel a shows a region where the difference between indium and gold can clearly be seen, the gold protected during plating by the photoresist and a thick non-uniform indium layer is grown. Panel b shows a region where beads of indium have grown but not yet come together to form one contiguous layer. In this region the gold pad has been etched away and taken some of the indium layer with it. By the photolithography pattern, indium should have grown inside a defined straight-line border here. It is likely that this area was not properly seeded by the initial direct current pulse prior to pulse-reverse plating. This particular region was farthest from the electrode and improper seeding leaves individual beads of indium surrounded by unprotected gold. This gold can be removed by the reverse-pulse of the plating cycle. Panels c and d show thick and continuous layers of indium. Notable features here are the craters which pit the surface of the indium. These features range in size up to ~10 µm in diameter. The craters are caused by hydrogen bubbles adhering to the indium surface. Hydrogen gas is a by-product of acidic electrodeposition and is readily produced on negatively-charged surfaces where H^+ ions in solution are attracted to the negatively-charged cathode and pair up to form H_2 gas. When stuck to the indium surface, the hydrogen bubbles prevent further indium growth, isolating the cathode form indium ions in the acidic solution. This leads to the crater features on the grown surface.

To prevent the uneven growth observed on the first test device, the gold pads were connected to the electroplating at multiple points, aiming to even out the current and charge distribution across the pads. The previous plating used only a single point of

electrical contact. Thus it is possible that the charge density and response to the pulsed current was inconsistent across the whole array. A magnetic stirrer was used to agitate the plating solution to reduce the size and number of hydrogen bubbles sticking to the cathode surface. The indium on this new chip was grown for 18 ks and electron microscopy images of the grown indium are show in Figure 5.4. Panels a and c show two different regions of the test chip with b and d showing the same respective regions with higher magnification. This chip was imaged before removing the photoresist so the gold lines between and surrounding the plating pads are not visible. The resist can be seen in the bright lines surrounding the indium at high magnification due to interactions between electron beam and resist. It is clear that the stirrer agitation was successful in reducing hydrogen bubble adhesion and size since neither region is pockmarked by the characteristic cratering pattern. The longer growth time and lack of cratering reveals a more amorphous layer of indium, with an estimated grain size of less than 10 µm. Exact grain size and layer thickness are difficult to estimate since the microscope scale bar is inaccurate when the beam is not perpendicular to the sample surface.

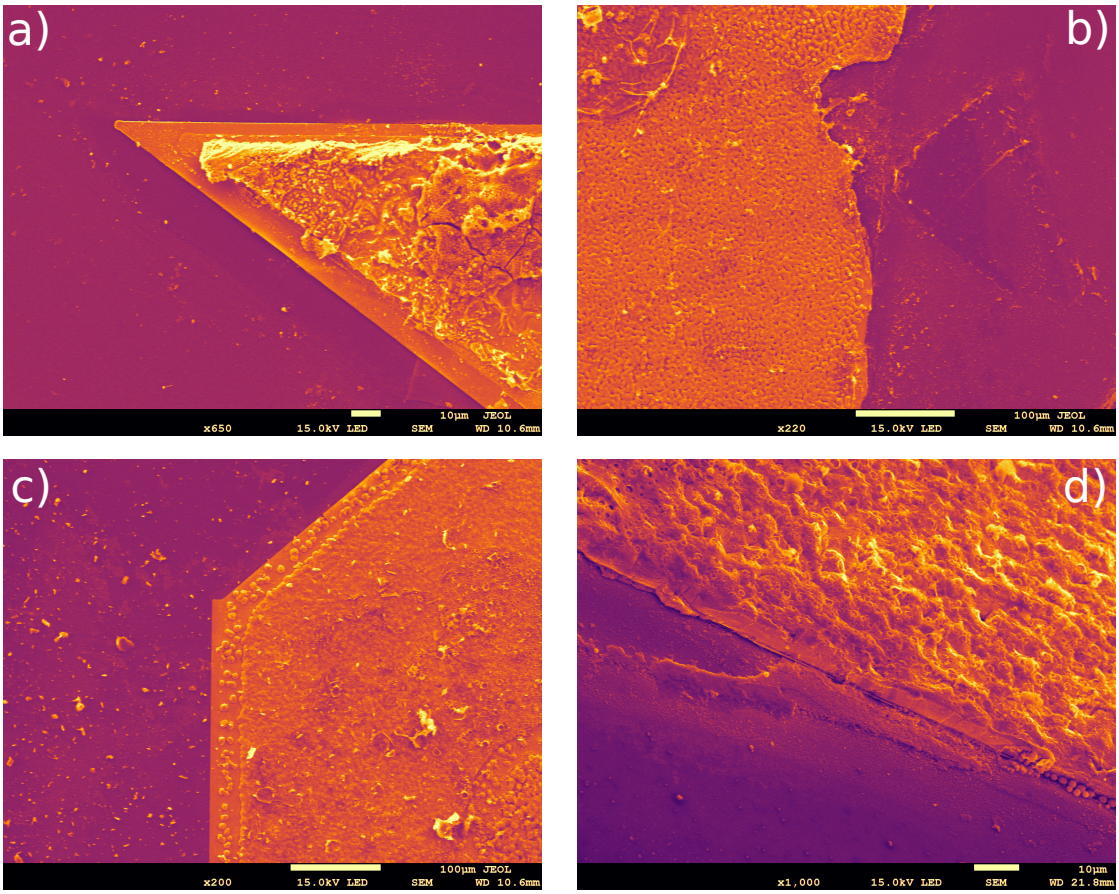

Figure 5.2: Four images of electroplated indium on the first test chip. Images are false-coloured to highlight changes in intensity. a) Clear separation of silicon, gold and indium layers. b) Beads of indium which have not yet joined to form one continuous layer. The gold base layer has been eaten away in parts. c)A uniform layer with hydrogen bubble cratering with craters up to 10 µm in diameter. d) An angled view of the edge of an indium layer. Gold appears to have been etched away next to this layer and the indium surface shows significant cratering.

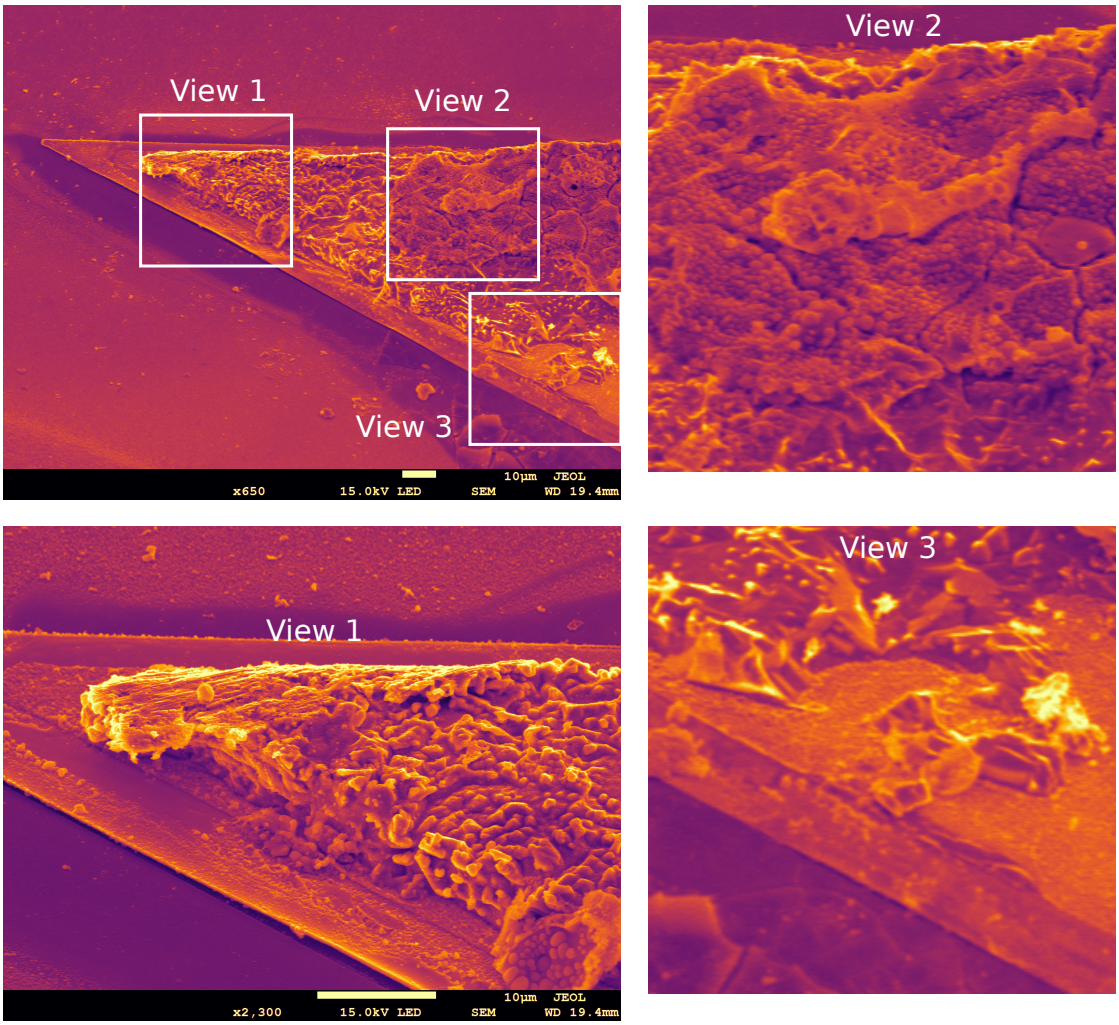

Figure 5.3: Higher magnification views of Figure 5.2 panel a. Images are taken from an angle to highlight layer thickness and false coloured to show changes in intensity. View 1 shows surface roughness, layer thickness and also a separation between gold which was protected by resist and gold seeded with indium. Evidence of skip-plating also shown in view 3 where indium was seeded but has not grown into a thick layer. View two is a thicker region of indium with a surface marked by beading, cratering and fissures.

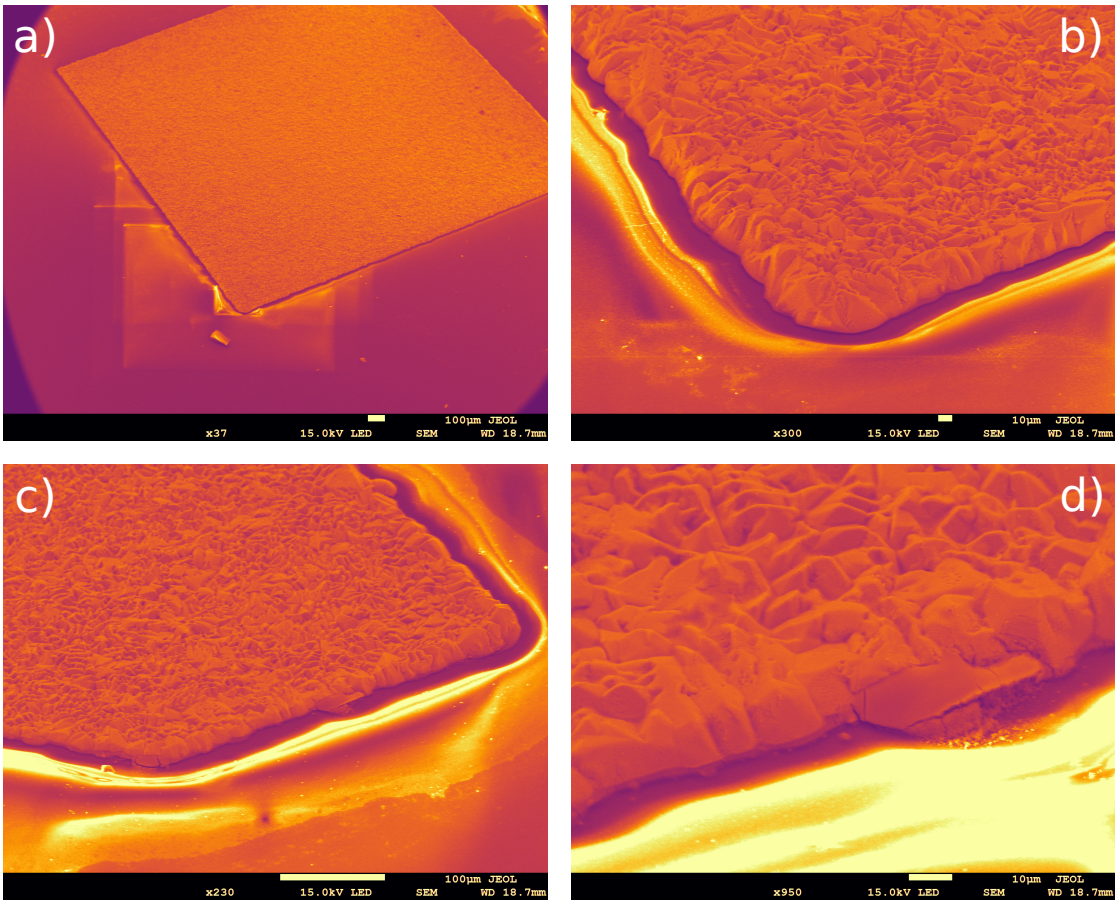

Figure 5.4: Electron microscope images of electroplated indium with optimised deposition settings. Images are false coloured to highlight intensity changes and taken from an angle to show layer thickness. Photoresist is still present on this images so some expected features, such as electrical lines between indium pads, are obscured. Panels a) and c) show two indium layers on two different pads on the same chip. b) and d) show the same respective layers in higher magnification. The cratering and uneven growth features observed on the previous test chip are notably absent. A clear grain-size of indium up to 10 µm in size can be seen.

5.4 Superconducting shells for probing helium

To diagnose issues in the indium electroplating process, the same chemical mix and pluse-reverse cycle was used to create superconducting indium shells. These shells were designed to be levitated and manipulated to study superfluid helium with a spherical probe. The spheroid nature of the probe is important since other resonators used to study helium often feature sharp edges and surface discontinuities which are suggested to impact their behaviour in helium [2]. Shells in particular were needed since a solid ball would be too heavy to levitate without fields significant enough to suppress indium superconductivity.

5.4.1 Electroplating a uniform sphere

Electrodeposition for nuclear refrigerant involves electroplating on 2D surfaces with these surfaces parallel to and equidistant from an indium anode. As such, each point on the surface should experience the same electric field generated by this anode, the same local charge density and thus be plated at the same rate. For a sphere this assumption breaks down. If a charge can be maintained on the sphere, the whole surface will be exposed to indium ions in solution and will be plated but not at the same rate. The rate depends on the local electric field on the sphere's surface and the local density of indium ions in solution. The point of the surface closest to the anode will be preferentially plated. That is of course ignoring the problem of maintaining an electrical charge on the sphere. Any electrode touching the sphere's surface will impede plating at that connection and any conductive surfaces on the electrode itself will also be plated. The growth of an indium will envelop and trap the electrode on the sphere's surface, joining electrode and sphere together.

The spheres we chose to plate were made of 1 mm Delrin plastic ball bearings which we coated in a 100 nm layer of silver via the Tollens test reaction. This left a conductive

shell on which we could deposit indium. The spheres were placed on a cathode formed of silver foil bent into a rough ”bowl” shape. This cathode was mechanically agitated during plating to encourage the spheres to roll and bounce around. This cathode was placed below a flat indium anode so that if the spheres bounced, they would fall back onto the cathode. The rolling and bouncing movement encouraged a more uniform growth on the spheres by constantly placing different parts of the surface in direct line-of-sight with the anode. Preliminary results of this plating are published in Arrayas et. al. [2].

Chapter 6

Conclusions and future work

6.1 Conclusions, summary and outlook

This thesis has described modelling and simulating the thermal dynamics of on-chip demagnetisation cooling. It has used this simulation to explore the numerous parameters which enable and harm cooling with this technique. Adiabatic nuclear demagnetisation of elements of nuclear refrigerant integrated into the circuitry of a nanoelectronic device is an emerging technique for cooling electrons into the microkelvin regime [22]. Heat flow through resistive links and electron-phonon coupling greatly diminish with lowering temperature. Cooling electrons to sub-millikelvin temperatures through these weakening links becomes increasingly difficult [88]. On-chip demagnetisation cooling was developed as a response to this, providing a direct electrical link between device and refrigerant.

Prior to this work, multiple teams have pursued microkelvin electron temperatures with on-chip demagnetisation cooling. There are few known thermometers which are sensitive to electron temperature in this range [14], which adds to the difficulty of investigating cooling. The teams have investigated Coulomb blockade thermometers [51] with integrated on-chip refrigerant [24]. In combination with off-chip adiabatic demagnetisation, these Coulomb blockade thermometers with on-chip cooling have measured electron temperatures as low as 421 ± 35 μK with indium refrigerant [27] and 224 ± 7 μK with copper. For experiments in Lancaster, Coulomb blockade thermometers have been cooled without off-chip demagnetisation. Only on-chip refrigerant has been used to cool below the dilution temperature of the host refrigerator [24]. With this approach, demagnetisation experiments in Lancaster have measured electron temperatures down to 1.0 ± 0.1 mK. The differences in approach observed temperatures are difficult to explain and reconcile. The need to understand thermalisation and cooling power of on-chip demagnetisation cooling is the motivation behind this study and its simulation.

In chapter 2 this work developed a first-principles thermal model of electronic thermalisation in on-chip refrigerant at low temperatures. This model presents a simple description of the thermal systems and links involved with on-chip cooling. In chapter 3, a simulation of on-chip cooling was built, based upon the thermal model. The simulation showed that Lancaster's experiments were limited by an increasing dilution refrigerator temperature. It also showed that cooling and temperatures in Coulomb blockade thermometers with integrated on-chip refrigerant are well captured by the simulation and first-principles thermal model.

There are numerous thermal links, material parameters and experiment environment conditions which can affect on-chip refrigeration. The simulation built in this work was used to perform a parameter-space exploration, described in chapter 4. The exploration found that refrigerator temperature is critical to the success of on-chip demagnetisation cooling. Electron-phonon coupling overwhelms demagnetisation cooling in a 10 mK refrigerator. There is a critical point around a temperature 3 mK for phonons internal to the refrigerant. Below this temperature electron-phonon coupling is sufficiently weak that nuclear cooling dominates. Above this phonon temperature, nuclear cooling potential is eroded by electron-phonon heat flow and cooling can be overwhelmed during demagnetisation. On-chip demagnetisation uses islands of refrigerant which are too small to generate significant eddy current heating when demagnetised. Demagnetising over the largest possible difference in field strength is desirable for lowering final electron temperatures. Parasitic heat leaks to the refrigerant should be reduced to below 0.1 fW to maximise cooling performance. The simulations find that, changing the refrigerant from copper to indium allows on-chip cooling to reach submillikelvin temperatures even in a in a 10 mK refrigerator, owing to the higher cooling power of indium. Further investigations of changing the refrigerant material are limited by a lack of literature values for the electron-phonon coupling constant in

many metals. Lastly, the simulation finds that electrons can be cooled to below 400 μK in a 10 mK dilution refrigerator with a copper refrigerant by increasing the Kapitza resistance between device and refrigerator. This increased resistance comes at a cost of longer pre-cooling times and in increased sensitivity to parasitic heat leaks.

Chapter 5 described the deposition and growth of magnetic refrigerant for on-chip cooling and attempts to cool a niobium nitride thermometer with this technique. Following on from the simulation's conclusions, indium was chosen as a suitable refrigerant. The challenges of electrodeposition held back the testing of this refrigerant with a thermometer but this work has presented a recipe and method for depositing indium refrigerant.

On-chip demagnetisation cooling is a proven technique for cooling electrons in Coulomb blockade thermometers to microkelvin temperatures. The natural future of this research is to integrate this cooling technique with other devices and thermometers, using low electron temperatures to explore new physics. With access to low electron temperatures in nanoelectronics, on-chip cooling can be used to investigate the electron-temperature dependence of new thermometers. Recent developments in thin-film resistors have shown niobium nitride to be a promising candidate for low temperature resistive thermometry [85]. Niobium atoms are randomly distributed throughout the material and incite an array of potential wells with random separation between wells. At millikelvin temperatures, the temperature-dependence of resistance can be described by Efros-Shkolvskii [84] variable range conductance [85]. NbN thin-film resistors are a promising example of an electron-sensitive thermometer.

6.2 Conclusions, summary and outlook

This thesis has described modelling and simulating the thermal dynamics of on-chip demagnetisation cooling. It has used this simulation to explore the numerous parameters which enable and harm cooling with this technique. Adiabatic nuclear demagnetisation of elements of nuclear refrigerant integrated into the circuitry of a nanoelectronic device is an emerging technique for cooling electrons into the microkelvin regime [22]. Heat flow through resistive links and electron-phonon coupling greatly diminish with lowering temperature. Cooling electrons to sub-millikelvin temperatures through these weakening links becomes increasingly difficult [88]. On-chip demagnetisation cooling was developed as a response to this, providing a direct electrical link between device and refrigerant.

Prior to this work, multiple teams have pursued microkelvin electron temperatures with on-chip demagnetisation cooling. There are few known thermometers which are sensitive to electron temperature in this range [14], which adds to the difficulty of investigating cooling. The teams have investigated Coulomb blockade thermometers [51] with integrated on-chip refrigerant [24]. In combination with off-chip adiabatic demagnetisation, these Coulomb blockade thermometers with on-chip cooling have measured electron temperatures as low as 421 ± 35 μK with indium refrigerant [27] and 224 ± 7 μK with copper. For experiments in Lancaster, Coulomb blockade thermometers have been cooled without off-chip demagnetisation. Only on-chip refrigerant has been used to cool below the dilution temperature of the host refrigerator [24]. With this approach, demagnetisation experiments in Lancaster have measured electron temperatures down to 1.0 ± 0.1 mK. The differences in approach observed temperatures are difficult to explain and reconcile. The need to understand thermalisation and cooling power of on-chip demagnetisation cooling is the motivation behind this study and its simulation.

In chapter 2 this work developed a first-principles thermal model of electronic thermalisation in on-chip refrigerant at low temperatures. This model presents a simple description of the thermal systems and links involved with on-chip cooling. In chapter 3, a simulation of on-chip cooling was built, based upon the thermal model. The simulation showed that Lancaster's experiments were limited by an increasing dilution refrigerator temperature. It also showed that cooling and temperatures in Coulomb blockade thermometers with integrated on-chip refrigerant are well captured by the simulation and first-principles thermal model.

There are numerous thermal links, material parameters and experiment environment conditions which can affect on-chip refrigeration. The simulation built in this work was used to perform a parameter-space exploration, described in chapter 4. The exploration found that refrigerator temperature is critical to the success of on-chip demagnetisation cooling. Electron-phonon coupling overwhelms demagnetisation cooling in a 10 mK refrigerator. There is a critical point around a temperature 3 mK for phonons internal to the refrigerant. Below this temperature electron-phonon coupling is sufficiently weak that nuclear cooling dominates. Above this phonon temperature, nuclear cooling potential is eroded by electron-phonon heat flow and cooling can be overwhelmed during demagnetisation. On-chip demagnetisation uses islands of refrigerant which are too small to generate significant eddy current heating when demagnetised. Demagnetising over the largest possible difference in field strength is desirable for lowering final electron temperatures. Parasitic heat leaks to the refrigerant should be reduced to below 0.1 fW to maximise cooling performance. The simulations find that, changing the refrigerant from copper to indium allows on-chip cooling to reach submillikelvin temperatures even in a in a 10 mK refrigerator, owing to the higher cooling power of indium. Further investigations of changing the refrigerant material are limited by a lack of literature values for the electron-phonon coupling constant in

many metals. Lastly, the simulation finds that electrons can be cooled to below 400 μK in a 10 mK dilution refrigerator with a copper refrigerant by increasing the Kapitza resistance between device and refrigerator. This increased resistance comes at a cost of longer pre-cooling times and in increased sensitivity to parasitic heat leaks.

Chapter 5 described the deposition and growth of magnetic refrigerant for on-chip cooling and attempts to cool a niobium nitride thermometer with this technique. Following on from the simulation's conclusions, indium was chosen as a suitable refrigerant. The challenges of electrodeposition held back the testing of this refrigerant with a thermometer but this work has presented a recipe and method for depositing indium refrigerant.

On-chip demagnetisation cooling is a proven technique for cooling electrons in Coulomb blockade thermometers to microkelvin temperatures. The natural future of this research is to integrate this cooling technique with other devices and thermometers, using low electron temperatures to explore new physics. With access to low electron temperatures in nanoelectronics, on-chip cooling can be used to investigate the electron-temperature dependence of new thermometers. Recent developments in thin-film resistors have shown niobium nitride to be a promising candidate for low temperature resistive thermometry [85]. Niobium atoms are randomly distributed throughout the material and incite an array of potential wells with random separation between wells. At millikelvin temperatures, the temperature-dependence of resistance can be described by Efros-Shkolvskii [84] variable range conductance [85]. NbN thin-film resistors are a promising example of an electron-sensitive thermometer.

References

[1] S. Autti *et al.*, "Thermal transport in nanoelectronic devices cooled by on-chip magnetic refrigeration," *Physical Review Letters*, vol. 131, no. 7, p. 077 001, Aug. 17, 2023. DOI: 10.1103/PhysRevLett.131.077001.

[2] M. Arrayás *et al.*, "Progress on levitating a sphere in cryogenic fluids," *Journal of Low Temperature Physics*, Feb. 4, 2023, ISSN: 1573-7357. DOI: 10.1007/s10909-022-02925-3.

[3] O. V. Lounasmaa, "Dilution refrigeration," *Journal of Physics E: Scientific Instruments*, vol. 12, no. 8, p. 668, Aug. 1979, ISSN: 0022-3735. DOI: 10.1088/0022-3735/12/8/001.

[4] P. Das, R. B. de Ouboter, and K. W. Taconis, "A realization of a london-clarke-mendoza type refrigerator," in *Low Temperature Physics LT9*, J. G. Daunt, D. O. Edwards, F. J. Milford, and M. Yaqub, Eds., Boston, MA: Springer US, 1965, pp. 1253–1255, ISBN: 978-1-4899-6443-4. DOI: 10.1007/978-1-4899-6443-4_133.

[5] O. V. Lounasmaa, *Experimental principles and methods below 1 K*. London ; New York: Academic Press, 1974, 316 pp., ISBN: 978-0-12-455950-9.

[6] C. Enss and S. Hunklinger, *Low-temperature physics*. Berlin ; New York: Springer, 2005, 573 pp., ISBN: 978-3-540-23164-6.

[7] D. J. Cousins *et al.*, "An advanced dilution refrigerator designed for the new lancaster microkelvin facility," *Journal of Low Temperature Physics*, vol. 114, no. 5, pp. 547–570, Mar. 1, 1999, ISSN: 1573-7357. DOI: 10.1023/A:1021862406629.

[8] A. H. Olafsdottir and H. U. Sverdrup, "Assessing the past and future sustainability of global helium resources, extraction, supply and use, using the integrated assessment model WORLD7," *Biophysical Economics and Sustainability*, vol. 5, no. 2, p. 6, May 19, 2020, ISSN: 2730-7204. DOI: 10.1007/s41247-020-00072-5.

[9] W. J. Nuttall, R. Clarke, and B. Glowacki, *The Future of Helium as a Natural Resource*. Routledge, Jun. 25, 2012, 370 pp., ISBN: 978-1-136-32273-0.

[10] P. Pari, "Dilution refrigerator with no liquid helium supply," in *Advances in Cryogenic Engineering: Part A & B*, ser. Advances in Cryogenic Engineering, R. W. Fast, Ed., Boston, MA: Springer US, 1990, pp. 1079–1086, ISBN: 978-1-4613-0639-9. DOI: 10.1007/978-1-4613-0639-9_130.

[11] K. Uhlig, ""dry" dilution refrigerator with pulse-tube precooling," *Cryogenics*, vol. 44, no. 1, pp. 53–57, Jan. 1, 2004, ISSN: 0011-2275. DOI: 10.1016/j.cryogenics.2003.07.007.

[12] H. Zu, W. Dai, and A. T. A. M. de Waele, "Development of dilution refrigerators—a review," *Cryogenics*, vol. 121, p. 103 390, Jan. 1, 2022, ISSN: 0011-2275. DOI: 10.1016/j.cryogenics.2021.103390.

[13] K. Uhlig, "Cryogen-free dilution refrigerators," *Journal of Physics: Conference Series*, vol. 400, no. 5, p. 052 039, Dec. 2012, ISSN: 1742-6596. DOI: 10.1088/1742-6596/400/5/052039.

[14] F. Giazotto, T. T. Heikkilä, A. Luukanen, A. M. Savin, and J. P. Pekola, "Opportunities for mesoscopics in thermometry and refrigeration: Physics and applications,"

Reviews of Modern Physics, vol. 78, no. 1, pp. 217–274, Mar. 17, 2006. DOI: 10.1103/RevModPhys.78.217.

[15] J. P. Pekola, "Towards quantum thermodynamics in electronic circuits," *Nature Physics*, vol. 11, no. 2, pp. 118–123, Feb. 2015, ISSN: 1745-2473, 1745-2481. DOI: 10.1038/nphys3169.

[16] F. Pobell, *Matter and Methods at Low Temperatures*. Berlin, Heidelberg: Springer, 2007, ISBN: 978-3-540-46356-6. DOI: 10.1007/978-3-540-46360-3.

[17] T. A. Knuuttila, J. T. Tuoriniemi, K. Lefmann, K. I. Juntunen, F. B. Rasmussen, and K. K. Nummila, "Polarized nuclei in normal and superconducting rhodium," *Journal of Low Temperature Physics*, vol. 123, no. 1, pp. 65–102, Apr. 1, 2001, ISSN: 1573-7357. DOI: 10.1023/A:1017545531677.

[18] M. L. Roukes, M. R. Freeman, R. S. Germain, R. C. Richardson, and M. B. Ketchen, "Hot electrons and energy transport in metals at millikelvin temperatures," *Physical Review Letters*, vol. 55, no. 4, pp. 422–425, Jul. 22, 1985. DOI: 10.1103/PhysRevLett.55.422.

[19] J. S. Xia, E. D. Adams, V. Shvarts, W. Pan, H. L. Stormer, and D. C. Tsui, "Ultra-low-temperature cooling of two-dimensional electron gas," *Physica B: Condensed Matter*, vol. 280, no. 1, pp. 491–492, May 11, 2000, ISSN: 0921-4526. DOI: 10.1016/S0921-4526(99)01843-8.

[20] N. Samkharadze, A. Kumar, M. J. Manfra, L. N. Pfeiffer, K. W. West, and G. A. Csáthy, "Integrated electronic transport and thermometry at milliKelvin temperatures and in strong magnetic fields," *Review of Scientific Instruments*, vol. 82, no. 5, p. 053 902, May 2011, ISSN: 0034-6748. DOI: 10.1063/1.3586766.

[21] D. I. Bradley *et al.*, "Nanoelectronic primary thermometry below 4 mK," *Nature Communications*, vol. 7, no. 1, p. 10 455, Jan. 27, 2016, ISSN: 2041-1723. DOI: 10.1038/ncomms10455.

[22] A. T. Jones, C. P. Scheller, J. R. Prance, Y. B. Kalyoncu, D. M. Zumbühl, and R. P. Haley, "Progress in cooling nanoelectronic devices to ultra-low temperatures," *Journal of Low Temperature Physics*, vol. 201, no. 5, pp. 772–802, Dec. 1, 2020, ISSN: 1573-7357. DOI: 10.1007/s10909-020-02472-9.

[23] L. A. Tracy *et al.*, "Single shot spin readout using a cryogenic high-electron-mobility transistor amplifier at sub-kelvin temperatures," *Applied Physics Letters*, vol. 108, no. 6, p. 063 101, Feb. 8, 2016, ISSN: 0003-6951. DOI: 10.1063/1.4941421.

[24] D. I. Bradley *et al.*, "On-chip magnetic cooling of a nanoelectronic device," *Scientific Reports*, vol. 7, no. 1, p. 45 566, Apr. 4, 2017, ISSN: 2045-2322. DOI: 10.1038/srep45566.

[25] M. Palma, C. P. Scheller, D. Maradan, A. V. Feshchenko, M. Meschke, and D. M. Zumbühl, "On-and-off chip cooling of a coulomb blockade thermometer down to 2.8 mK," *Applied Physics Letters*, vol. 111, no. 25, p. 253 105, Dec. 18, 2017, ISSN: 0003-6951. DOI: 10.1063/1.5002565.

[26] N. Yurttagül, M. Sarsby, and A. Geresdi, "Indium as a high-cooling-power nuclear refrigerant for quantum nanoelectronics," *Physical Review Applied*, vol. 12, no. 1, p. 011 005, Jul. 31, 2019. DOI: 10.1103/PhysRevApplied.12.011005.

[27] M. Sarsby, N. Yurttagül, and A. Geresdi, "500 microkelvin nanoelectronics," *Nature Communications*, vol. 11, no. 1, p. 1492, Mar. 20, 2020, ISSN: 2041-1723. DOI: 10.1038/s41467-020-15201-3.

[28] M. Samani *et al.*, "Microkelvin electronics on a pulse-tube cryostat with a gate coulomb-blockade thermometer," *Physical Review Research*, vol. 4, no. 3, p. 033 225, Sep. 19, 2022. DOI: 10.1103/PhysRevResearch.4.033225.

[29] A. Smith, "Who discovered the magnetocaloric effect?" *The European Physical Journal H*, vol. 38, no. 4, pp. 507–517, Sep. 1, 2013, ISSN: 2102-6467. DOI: 10.1140/epjh/e2013-40001-9.

[30] R. P. Hudson, *Principles and application of magnetic cooling* (North-Holland series in low temperature physics v. 2). Amsterdam: North-Holland Pub. Co, 1972, 230 pp., ISBN: 978-0-7204-1257-4.

[31] A. Vlasov, J. Guillemette, G. Gervais, and T. Szkopek, "Magnetic refrigeration with paramagnetic semiconductors at cryogenic temperatures," *Applied Physics Letters*, vol. 111, no. 14, p. 142 102, Oct. 2017. DOI: 10.1063/1.4994536.

[32] S. Abe and K. Matsumoto, "Nuclear demagnetization for ultra-low temperatures," *Cryogenics*, vol. 62, pp. 213–220, Jul. 2014. DOI: 10.1016/j.cryogenics.2014.04.004.

[33] I. Todoshchenko, J.-P. Kaikkonen, R. Blaauwgeers, P. J. Hakonen, and A. Savin, "Dry demagnetization cryostat for sub-millikelvin helium experiments: Refrigeration and thermometry," *Review of Scientific Instruments*, vol. 85, no. 8, p. 085 106, Aug. 5, 2014, ISSN: 0034-6748. DOI: 10.1063/1.4891619.

[34] J. Nyéki *et al.*, "High-performance cryogen-free platform for microkelvin-range refrigeration," *Physical Review Applied*, vol. 18, no. 4, p. L041002, Oct. 24, 2022. DOI: 10.1103/PhysRevApplied.18.L041002.

[35] P. J. Shirron, "Applications of the magnetocaloric effect in single-stage, multi-stage and continuous adiabatic demagnetization refrigerators," *Cryogenics*, vol. 62,

pp. 130–139, Jul. 1, 2014, ISSN: 0011-2275. DOI: 10.1016/j.cryogenics.2014.03.014.

[36] D. Schmoranzer, R. Gazizulin, S. Triqueneaux, E. Collin, and A. Fefferman, "Development of a sub-mK continuous nuclear demagnetization refrigerator," *Journal of Low Temperature Physics*, vol. 196, no. 1, pp. 261–267, Jul. 1, 2019, ISSN: 1573-7357. DOI: 10.1007/s10909-018-02128-9.

[37] D. Schmoranzer, J. Butterworth, S. Triqueneaux, E. Collin, and A. Fefferman, "Design evaluation of serial and parallel sub-mK continuous nuclear demagnetization refrigerators," *Cryogenics*, vol. 110, p. 103 119, Sep. 1, 2020, ISSN: 0011-2275. DOI: 10.1016/j.cryogenics.2020.103119.

[38] K. A. Gschneidner and V. K. Pecharsky, "Thirty years of near room temperature magnetic cooling: Where we are today and future prospects," *International Journal of Refrigeration*, vol. 31, no. 6, pp. 945–961, Sep. 1, 2008, ISSN: 0140-7007. DOI: 10.1016/j.ijrefrig.2008.01.004.

[39] M. T. Huiku, T. A. Jyrkkiö, J. M. Kyynäräinen, A. S. J. Oja, K. N. Clausen, and M. Steiner, "Nuclear magnetic ordering in copper: Present knowledge and future experiments," *Physica Scripta*, vol. 1986, p. 114, T13 Jan. 1986, ISSN: 1402-4896. DOI: 10.1088/0031-8949/1986/T13/018.

[40] N. Kurti, F. N. H. Robinson, F. Simon, and D. A. Spohr, "Nuclear cooling," *Nature*, vol. 178, no. 4531, pp. 450–453, Sep. 1956, ISSN: 1476-4687. DOI: 10.1038/178450a0.

[41] P. M. Echternach, M. R. Thoman, C. M. Gould, and H. M. Bozler, "Electron-phonon scattering rates in disordered metallic films below 1 k," *Physical Review B*, vol. 46, no. 16, pp. 10 339–10 344, Oct. 15, 1992. DOI: 10.1103/PhysRevB.46.10339.

[42] F. C. Wellstood, C. Urbina, and J. Clarke, "Hot-electron effects in metals," *Physical Review B*, vol. 49, no. 9, pp. 5942–5955, Mar. 1, 1994. DOI: 10.1103/PhysRevB.49.5942.

[43] L. Casparis *et al.*, "Metallic coulomb blockade thermometry down to 10 mK and below," *Review of Scientific Instruments*, vol. 83, no. 8, p. 083 903, Aug. 15, 2012, ISSN: 0034-6748. DOI: 10.1063/1.4744944.

[44] N. Yurttagul, "Microkelvin nanoelectronics," Ph.D. dissertation, Delft University of Technology, 2020. DOI: 10.4233/UUID:5A57DF7E-682C-458A-8C28-45AE96C40D7B.

[45] A. C. Anderson, "The kapitza thermal boundary resistance between two solids," in *Nonequilibrium Superconductivity, Phonons, and Kapitza Boundaries*, ser. NATO Advanced Study Institutes Series, K. E. Gray, Ed., Boston, MA: Springer US, 1981, pp. 1–30, ISBN: 978-1-4684-3935-9. DOI: 10.1007/978-1-4684-3935-9_1.

[46] A. C. Anderson and R. E. Peterson, "The thermal resistance between electrons and phonons in copper," *Physics Letters A*, vol. 38, no. 7, pp. 519–520, Mar. 27, 1972, ISSN: 0375-9601. DOI: 10.1016/0375-9601(72)90797-9.

[47] J. Chen, X. Xu, J. Zhou, and B. Li, "Interfacial thermal resistance: Past, present, and future," *Reviews of Modern Physics*, vol. 94, no. 2, p. 025 002, Apr. 22, 2022. DOI: 10.1103/RevModPhys.94.025002.

[48] E. T. Swartz and R. O. Pohl, "Thermal boundary resistance," *Reviews of Modern Physics*, vol. 61, no. 3, pp. 605–668, Jul. 1, 1989. DOI: 10.1103/RevModPhys.61.605.

[49] D. Bradley *et al.*, "Magnetic phase transition in a nanonetwork of solid he3 in aerogel," *Physical Review Letters*, vol. 105, no. 12, 2010, ISSN: 1079-7114. DOI: 10.1103/PhysRevLett.105.125303.

[50] N. W. Ashcroft and N. D. Mermin, *Solid state physics*. New York: Holt, Rinehart and Winston, 1976, 826 pp., ISBN: 978-0-03-083993-1.

[51] M. Meschke, J. P. Pekola, F. Gay, R. E. Rapp, and H. Godfrin, "Electron thermalization in metallic islands probed by coulomb blockade thermometry," *Journal of Low Temperature Physics*, vol. 134, no. 5, pp. 1119–1143, Mar. 1, 2004, ISSN: 1573-7357. DOI: 10.1023/B:JOLT.0000016733.75220.5d.

[52] Y. Koike, H. Suzuki, S. Abe, Y. Karaki, M. Kubota, and H. Ishimoto, "Ferromagnetic nuclear spin order of scandium," *Journal of Low Temperature Physics*, vol. 101, no. 3, pp. 617–622, Nov. 1, 1995, ISSN: 1573-7357. DOI: 10.1007/BF00753363.

[53] J. Leib, M. Huebner, S. Götz, T. Wagner, and G. Eska, "NMR-investigations on thallium-samples of high spin-polarization," *Journal of Low Temperature Physics*, vol. 101, no. 1, pp. 253–258, Oct. 1, 1995, ISSN: 1573-7357. DOI: 10.1007/BF00754585.

[54] J. P. Pekola, K. P. Hirvi, J. P. Kauppinen, and M. A. Paalanen, "Thermometry by arrays of tunnel junctions," *Physical Review Letters*, vol. 73, no. 21, pp. 2903–2906, Nov. 21, 1994. DOI: 10.1103/PhysRevLett.73.2903.

[55] A. Jones, "Cooling electrons in nanoelectronic devices by on-chip demagnetisation," Ph.D. dissertation, Lancaster University, 2019.

[56] P. L. Kapitza, "Heat transfer and superfluidity of helium II," *Physical Review*, vol. 60, no. 4, pp. 354–355, Aug. 15, 1941. DOI: 10.1103/PhysRev.60.354.

[57] J. P. Harrison, "Review paper: Heat transfer between liquid helium and solids below 100 mK," *Journal of Low Temperature Physics*, vol. 37, no. 5, pp. 467–565, Dec. 1, 1979, ISSN: 1573-7357. DOI: 10.1007/BF00113870.

[58] Y. M. Bunkov *et al.*, "A compact dilution refrigerator with vertical heat exchangers for operation to 2 mK," *Journal of Low Temperature Physics*, vol. 83, no. 5, pp. 257–272, Jun. 1, 1991, ISSN: 1573-7357. DOI: 10.1007/BF00683626.

[59] L. V. Levitin *et al.*, "Cooling low-dimensional electron systems into the microkelvin regime," *Nature Communications*, vol. 13, no. 1, p. 667, Feb. 3, 2022, ISSN: 2041-1723. DOI: 10.1038/s41467-022-28222-x.

[60] G. Nicolí *et al.*, "Quantum dot thermometry at ultra-low temperature in a dilution refrigerator with a 4he immersion cell," *Review of Scientific Instruments*, vol. 90, no. 11, p. 113 901, Nov. 13, 2019, ISSN: 0034-6748. DOI: 10.1063/1.5127830.

[61] H. J. Goldsmid, *The Physics of Thermoelectric Energy Conversion:* Morgan & Claypool Publishers, Apr. 1, 2017, ISBN: 978-1-68174-641-8. DOI: 10.1088/978-1-6817-4641-8.

[62] H. Goldsmid and G. Nolas, "A review of the new thermoelectric materials," in *Proceedings ICT2001. 20 International Conference on Thermoelectrics (Cat. No.01TH8589)*, Jun. 2001, pp. 1–6. DOI: 10.1109/ICT.2001.979602.

[63] J. Pekola, R. Schoelkopf, and J. Ullom, "Cryogenics on a chip," *Physics Today*, vol. 57, no. 5, pp. 41–47, May 1, 2004, ISSN: 0031-9228. DOI: 10.1063/1.1768673.

[64] H. J. Goldsmid and A. S. Gray, "Thermoelectric refrigeration at very low temperatures," *Cryogenics*, vol. 19, no. 5, pp. 289–292, May 1, 1979, ISSN: 0011-2275. DOI: 10.1016/0011-2275(79)90146-2.

[65] A. Kapitulnik, "Thermoelectric cooling at very low temperatures," *Applied Physics Letters*, vol. 60, no. 2, pp. 180–182, Jan. 13, 1992, ISSN: 0003-6951. DOI: 10.1063/1.106956.

[66] J. T. Muhonen, M. Meschke, and J. P. Pekola, "Micrometre-scale refrigerators," *Reports on Progress in Physics*, vol. 75, no. 4, p. 046 501, Mar. 2012, ISSN: 0034-4885. DOI: 10.1088/0034-4885/75/4/046501.

[67] J. R. Prance *et al.*, "Electronic refrigeration of a two-dimensional electron gas," *Physical Review Letters*, vol. 102, no. 14, p. 146 602, Apr. 6, 2009. DOI: 10.1103/PhysRevLett.102.146602.

[68] S.-Y. Hwang, B. Sothmann, and D. Sánchez, "Superconductor–quantum dot hybrid coolers," *Physical Review B*, vol. 107, no. 24, p. 245 412, Jun. 9, 2023. DOI: 10.1103/PhysRevB.107.245412.

[69] S. Gasparinetti, F. Deon, G. Biasiol, L. Sorba, F. Beltram, and F. Giazotto, "Probing the local temperature of a two-dimensional electron gas microdomain with a quantum dot: Measurement of electron-phonon interaction," *Physical Review B*, vol. 83, no. 20, p. 201 306, May 18, 2011. DOI: 10.1103/PhysRevB.83.201306.

[70] A. Kemppinen, A. Ronzani, E. Mykkänen, J. Hätinen, J. S. Lehtinen, and M. Prunnila, "Cascaded superconducting junction refrigerators: Optimization and performance limits," *Applied Physics Letters*, vol. 119, no. 5, p. 052 603, Aug. 5, 2021, ISSN: 0003-6951. DOI: 10.1063/5.0060652.

[71] E. Mykkänen *et al.*, "Thermionic junction devices utilizing phonon blocking," *Science Advances*, vol. 6, no. 15, Apr. 2020. DOI: 10.1126/sciadv.aax9191.

[72] P. Virtanen *et al.*, "SciPy 1.0: Fundamental algorithms for scientific computing in python," *Nature Methods*, vol. 17, no. 3, pp. 261–272, Mar. 2020, ISSN: 1548-7105. DOI: 10.1038/s41592-019-0686-2.

[73] L. Petzold, "Automatic selection of methods for solving stiff and nonstiff systems of ordinary differential equations," *SIAM Journal on Scientific and Statistical*

Computing, vol. 4, no. 1, pp. 136–148, Mar. 1983, ISSN: 0196-5204. DOI: 10.1137/0904010.

[74] V. I. Khvesyuk, B. Liu, and A. A. Barinov, "A new look at kapitza conductance calculation (thermal boundary resistance)," *Journal of Physics: Conference Series*, vol. 1368, no. 4, p. 042 035, Nov. 2019, ISSN: 1742-6596. DOI: 10.1088/1742-6596/1368/4/042035.

[75] D. A. Young and H. J. Maris, "Lattice-dynamical calculation of the kapitza resistance between fcc lattices," *Physical Review B*, vol. 40, no. 6, pp. 3685–3693, Aug. 15, 1989. DOI: 10.1103/PhysRevB.40.3685.

[76] A. Meilakhs and B. Semak, "Calculation of kapitza resistance with kinetic equation," *physica status solidi (b)*, vol. 258, no. 8, p. 2 100 018, 2021, ISSN: 1521-3951. DOI: 10.1002/pssb.202100018.

[77] J. Engert *et al.*, "Practical noise thermometers for low temperatures," *Journal of Physics: Conference Series*, vol. 150, no. 1, p. 012 012, Feb. 2009, ISSN: 1742-6596. DOI: 10.1088/1742-6596/150/1/012012.

[78] A. Casey *et al.*, "Current sensing noise thermometry: A fast practical solution to low temperature measurement," *Journal of Low Temperature Physics*, vol. 175, no. 5, pp. 764–775, Jun. 1, 2014, ISSN: 1573-7357. DOI: 10.1007/s10909-014-1147-z.

[79] A. Shibahara *et al.*, "Primary current-sensing noise thermometry in the millikelvin regime," *Philosophical Transactions of the Royal Society A: Mathematical, Physical and Engineering Sciences*, vol. 374, no. 2064, p. 20 150 054, Mar. 28, 2016. DOI: 10.1098/rsta.2015.0054.

[80] J. B. Johnson, "Thermal agitation of electricity in conductors," *Physical Review*, vol. 32, no. 1, pp. 97–109, Jul. 1, 1928. DOI: 10.1103/PhysRev.32.97.

[81] H. Nyquist, "Thermal agitation of electric charge in conductors," *Physical Review*, vol. 32, no. 1, pp. 110–113, Jul. 1, 1928. DOI: 10.1103/PhysRev.32.110.

[82] P. W. Anderson, "Absence of diffusion in certain random lattices," *Physical Review*, vol. 109, no. 5, pp. 1492–1505, Mar. 1, 1958. DOI: 10.1103/PhysRev.109.1492.

[83] R. Abou-Chacra, D. J. Thouless, and P. W. Anderson, "A selfconsistent theory of localization," *Journal of Physics C: Solid State Physics*, vol. 6, no. 10, p. 1734, May 1973, ISSN: 0022-3719. DOI: 10.1088/0022-3719/6/10/009.

[84] A. L. Efros and B. I. Shklovskii, "Coulomb gap and low temperature conductivity of disordered systems," *Journal of Physics C: Solid State Physics*, vol. 8, no. 4, p. L49, Feb. 1975, ISSN: 0022-3719. DOI: 10.1088/0022-3719/8/4/003.

[85] T. Nguyen *et al.*, "Niobium nitride thin films for very low temperature resistive thermometry," *Journal of Low Temperature Physics*, vol. 197, no. 5, pp. 348–356, Dec. 1, 2019, ISSN: 1573-7357. DOI: 10.1007/s10909-019-02222-6.

[86] J. A. Slattery, "Indium plating," *Metal Finishing*, vol. 100, pp. 250–252, Jan. 2002. DOI: 10.1016/s0026-0576(02)82025-6.

[87] T. Yingtao, "Electrodeposition of indium bumps for ultrafine pitch interconnections," Ph.D. dissertation, Loughborough University, 2010.

[88] Z. Iftikhar *et al.*, "Primary thermometry triad at 6 mK in mesoscopic circuits," *Nature Communications*, vol. 7, no. 1, p. 12 908, Sep. 23, 2016, ISSN: 2041-1723. DOI: 10.1038/ncomms12908.